JOURNAL OF GEOPHYSICAL RESEARCH, VOL. 115, B07303, doi:10.1029/2008JB006079, 2010



# Mantle structure beneath the western United States and its implications for convection processes

Mei Xue[1,2] and Richard M. Allen[2]

Received 6 September 2008; revised 20 July 2009; accepted 22 February 2010; published 13 July 2010.

[1] We present tomographic images of the mantle structure beneath the western United States. Our Dynamic North America Models of P and S velocity structure (DNA07-P and DNA07-S) use teleseismic body waves recorded at ~600 seismic stations provided by the Earthscope Transportable Array and regional networks. DNA07-P and -S benefit from the unprecedented aperture of the network while maintaining a dense station distribution providing high-resolution body wave imaging of features through the transition zone and into the lower mantle. The main features imaged include (1) the Juan de Fuca subduction system that bottoms at ~400 km beneath Oregon, implying interaction with the Yellowstone anomaly; (2) a low-velocity conduit beneath Yellowstone National Park that bottoms at 500 km and dips toward the northwest; (3) shallow low-velocity anomalies (upper 200 km) beneath the eastern Snake River Plain (ESRP) and the High Lava Plains, and a deep low-velocity anomaly (>600 km) beneath the ESRP but not Newberry; (4) a low-velocity "slab gap" to ~400 km depth immediately south of the Mendocino Triple Junction and south of the Gorda slab; and (5) high-velocity "drips" beneath the Transverse Ranges, the southern Central Valley/Sierra Nevada, and central Nevada. These observations reveal extremely heterogeneous mantle structure for the western United States and suggest that we are only just beginning to image the complex interactions between geologic objects. The transportable array allows for analysis of the relationships between these anomalies in an internally consistent single tomographic model. The DNA velocity models are available for download and slicing at http://dna.berkeley.edu.

**Citation:** Xue, M., and R. M. Allen (2010), Mantle structure beneath the western United States and its implications for convection processes, *J. Geophys. Res.*, *115*, B07303, doi:10.1029/2008JB006079.

## 1. Introduction

[2] The western United States is on the margin of the North American plate and is a region that has complicated and active tectonics. The Juan de Fuca plate, the Pacific plate, and the North American plate meet in this region and form the Mendocino triple junction just offshore northern California (Figure 1). North of the triple junction, the Juan de Fuca plate is subducting beneath the North American plate from the northwest. South of the triple junction is the strike-slip San Andreas Fault, the plate boundary between the Pacific and North American plates.

[3] The Juan de Fuca plate is a remnant of the much larger Farallon plate. Around 30 Ma, when the ridge separating the Farallon and Pacific plates reached the North American plate, the Farallon plate was then split into two major subplates, separated by the San Andreas Fault. The Juan de Fuca plate is the central part of the northern subplate with the Explorer plate to its north and the Gorda plate to its south [*Severinghaus and Atwater*, 1990]. Here we refer to all three subplates as the Juan de Fuca plate. The maximum compressive stress observed for the Juan de Fuca plate is along N-S direction in the southernmost region and in a NE-SW to E-W direction off Oregon, which are primarily a result of the right lateral shear motion of the Pacific and North America plates [*Wang et al.*, 1997]. Due to its proximity to the Juan de Fuca Ridge to the west, the Juan de Fuca plate being subducted is young, ~10 Ma old [*Severinghaus and Atwater*, 1990], and is expected to have positive S velocity anomalies of ~2% to 4% at depths greater than 400 km [*Xue and Allen*, 2007]. In previous studies, the Juan de Fuca slab was imaged to depths of ~300 to 400 km beneath Washington but was absent in the mantle east of the Cascades beneath Oregon [e.g., *Michaelson and Weaver*, 1986; *Rasmussen and Humphreys*, 1988; *Harris et al.*, 1991; *Bostock et al.*, 2002]. A recent seismic traveltime tomographic model using the same methodology as this study but focused in Oregon imaged the Juan de Fuca slab dipping ~50°E to a depth of ~400 km in the mantle east of the Cascades beneath Oregon but no deeper [*Xue and Allen*, 2007]. The slab imaged above represents the currently actively subducting remnant of the Farallon plate. It was broken off from the deeper part, the

[1]State Key Laboratory of Marine Geology, School of Ocean and Earth Science, Tongji University, Shanghai, China.
[2]Department of Earth and Planetary Sciences, University of California, Berkeley, California, USA.


0148-0227/10/2008JB006079

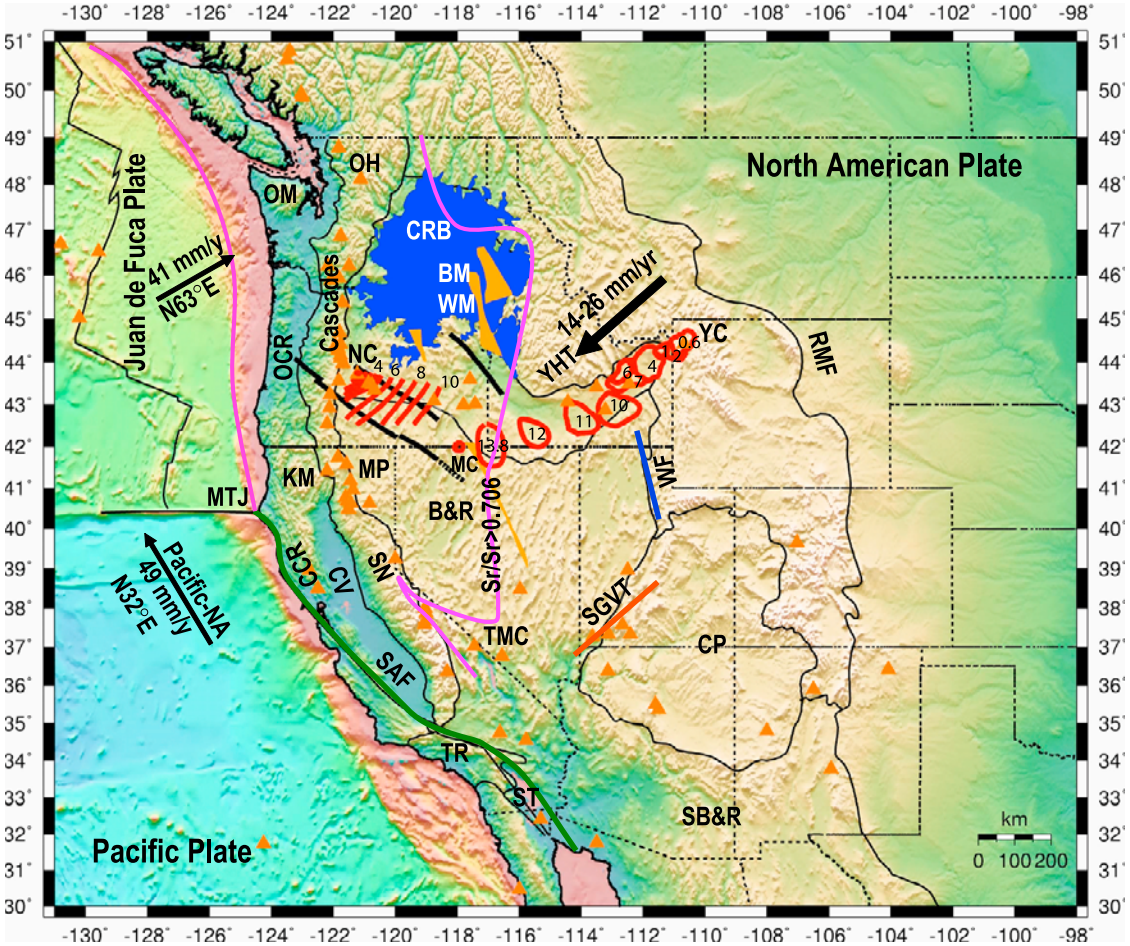


**Figure 1.** Tectonic map for the study region. Labeled features [*Humphreys and Dueker*, 1994b] are OH, Okanogan Highlands; OM, Olympic Mountains; OCR, Oregon Coast Ranges; CCR, California Coast Ranges; KM, Klamath Mountains; MP, Modoc Plateau; MTJ, Mendocino Triple Junction; CV, Central Valley; SN, Sierra Nevada; SAF, San Andreas Fault; TR, Transverse Ranges; ST, Salton Trough; CRB, Columbia River Basalts; BM, Blue Mountains; WM, Wallowa Mountains; NC, Newberry caldera; MC, McDermitt caldera; YC, Yellowstone caldera; YHT, Yellowstone hot spot track along the eastern Snake River Plain; B&R, Basin and Range; SB&R, southern Basin and Range; TMC, Timber Mountain caldera; SGVT, Saint George Volcanic Trend; CP, Colorado Plateau; WF, Wasatch Front; RMF, Rocky Mountain Front. Black lines trending northwest across Oregon indicates right lateral strike-slip faults. Dike swarms associated with the 17 Ma basaltic outpourings are shown in gold [*Christiansen et al.*, 2002]. Age contours of initial rhyolitic volcanism along the Newberry track are shown as thick red lines in 1 Ma increments extending to the Newberry caldera [*Jordan et al.*, 2004]. Major rhyolitic caldera centers along the Yellowstone track are shown as red circles with age in Ma extending to the Yellowstone caldera [*Pierce and Morgan*, 1992]. Both the Newberry and Yellowstone tracks initiate in the region of the McDermitt caldera, which is shown as a red circle. Plate motions from HS3-NUVEL 1A are shown as black arrows [*Gripp and Gordon*, 2002].

previously flat Farallon subduction, deepening the dip angle. The break might be caused by collision of the subducted Farallon plate along the edge of the craton ~1,000 km inland [*Sigloch et al.*, 2008]. The extreme flattening of the Farallon subduction has been proposed as a possible cause of the Laramide compression (75–50 Ma) [*Dickinson and Snyder*, 1978; *Tikoff and Maxson*, 2001].

[4] Besides the Juan de Fuca subduction system, many other complicated geologic features are also observed in the western United States. The most prominent features are the voluminous volcanism that initiated around 16Ma to 17Ma: the Yellowstone hot spot track, the Columbia River Basalts, and the Newberry hot spot track (Figure 1). The Yellowstone hot spot track is associated with northeastward migration of silicic volcanism along the eastern Snake River Plain ending at the Yellowstone caldera [e.g., *Pierce and Morgan*, 1992; *Smith and Braile*, 1994] (Figure 1). The Columbia River basalts extend throughout eastern Oregon, eastern Washington, and western Idaho, and are a series of flows with ages primarily 17–14 Ma [e.g., *Christiansen et al.*, 2002]. The Newberry hot spot track, along the Oregon High Lava Plains, consists of a sequence of volcanic rhyolitic domes showing a monotonic age progression from ~17 Ma trending northwest ending at the Newberry caldera where ages are younger than

0.01 Ma (Figure 1) [*Jordan*, 2005]. Both the Newberry and Yellowstone tracks initiated from a region near the McDermitt caldera around ~17 Ma.

[5] The formation of the Yellowstone hot spot track has been proposed to be a mantle plume impacting the North American lithosphere around 17 Ma. This plume hypothesis is supported by the following observations [*Waite et al.*, 2006]: (1) the well-defined track of progressively older silicic volcanism in the direction of plate motion; (2) a parabolic pattern of high topography and seismicity distribution [*Anders et al.*, 1989; *Pierce and Morgan*, 1992; *Smith and Braile*, 1994]; (3) a 10 to 12 m positive geoid anomaly with a 500 km radius centered at Yellowstone [*Smith and Braile*, 1994]; and (4) high $^3He/^4He$ ratios up to 16 Ra at Yellowstone from 3 Ra immediately outside the caldera [*Fournier*, 1989, and references therein], where Ra is the atmospheric value of $1.38 \times 10^{-6}$; (5) high heat flow averaging more than 1700 mW/m2 was observed within the youngest 0.64 Ma and 3000 km$^2$ caldera [*Blackwell*, 1969]. These observations of the parabolic topography, high heat flow, and the elevated $He^3/He^4$ ratio are predicted characteristics of deep mantle plumes [*Sleep*, 1990; *Hill et al.*, 1992; *Ribe and Christensen*, 1994]. High ratios of $^3He/^4He$ (>10 Ra) are generally taken as indicators of lower mantle components [e.g., *Craig et al.*, 1978] based on a standard model, where upper mantle is depleted, degassed, and homogenized, while lower mantle is little degassed or undegassed and contains much more $^3He$ than the upper mantle (D. L. Anderson et al., Helium: Fundamental models, 2006, www.MantlePlumes.org). However, processes have also been proposed to explain the presence of high $^3He/^4He$ ratios in the upper mantle [*Anderson*, 1998]. Clear evidence for the presence or absence of an upwelling conduit through the lower mantle beneath Yellowstone remains elusive and the debate continues as to whether a mantle plume is the origin [e.g., *Humphreys et al.*, 2000; *Yuan and Dueker*, 2005; *Waite et al.*, 2006].

[6] As a large igneous province with an estimated volume of 174,300 km$^3$ [*Chesley and Ruiz*, 1998], the source of the Columbia River Basalts (CRB) is still under debate. Some studies have attributed the source of CRB to the Yellowstone deep mantle plume [e.g., *Geist and Richards*, 1993; *Pierce et al.*, 2000b] or a plume-triggered delamination [*Camp and Hanan*, 2008]. However, an alternative causal mechanism which requires no deep mantle plume has also been proposed for the Columbia River flood basalts. *Hales et al.* [2005] propose that delamination of the Wallowa plutonic roots could be responsible for the voluminous outpouring [*Hales et al.*, 2005].

[7] While some studies attribute the source of the Newberry hot spot track to be the Yellowstone plume [e.g., *Draper*, 1991], other studies use the northwest propagating Newberry hot spot track to disfavor the Yellowstone plume hypothesis all together [e.g., *Christiansen et al.*, 2002]. Alternative causal mechanisms for Newberry include subduction counterflow, gravitational flow along lithospheric topography of the North American craton, and lithospheric fracturing [e.g., *Smith*, 1977; *Draper*, 1991; *Humphreys et al.*, 2000; *Pierce et al.*, 2000a; *Christiansen et al.*, 2002; *Jordan*, 2005]. Seismic anisotropy beneath the Newberry track suggests no flow along the length of the track implying that lithospheric processes are the most likely cause [*Xue and Allen*, 2006]. Therefore, the Newberry hot spot track itself cannot be used to argue for or against the Yellowstone Plume hypothesis.

[8] Given the proximity of the slab and the proposed Yellowstone Plume it is likely that the subduction and the upwelling processes interact with one another [e.g., *Geist and Richards*, 1993; *Pierce et al.*, 2000b]. The JdF07 model [*Xue and Allen*, 2007] imaged the subducted Juan de Fuca plate in the mantle east of the Cascades beneath Oregon but found it stops at a depth of 400 km. Accordingly, *Xue and Allen* [2007] propose that the absence of the slab below 400 km today is due to the arrival of the Yellowstone plume head at ~17 Ma, which destroyed the Juan de Fuca slab at depths greater than the thickness of the continental lithosphere.

[9] In addition to these primary tectonic objects and volcanic processes described above, there are several other prominent geologic provinces in the western United States shown in Figure 1. To the west is the Coastal Ranges (Oregon Coastal Range and California Coastal Range specifically), a mountain belt following the coastline from the Olympic Mountains of Washington south to the westernmost Transverse Ranges in southern California. The Oregon Coastal Range likely began as an ocean island chain that collided with the continental tectonic plate of North America more than 60 million years ago meaning that the oldest portions of the Oregon Coastal Range are over 60 million years old [*Orr et al.*, 1992]. The California Coastal Ranges are much younger and were formed 3 to 4 million years ago when the Pacific Plate began to move obliquely past the North American Plate. This caused some convergence between the plates generating the mountains [*Harden*, 1998]. Immediately east of the Oregon Coastal Ranges is the Cascades extending from Okanogan Highlands in Washington south to the northern California Coastal Ranges. The Cascades delineate the active volcanic arc related to the Juan de Fuca subduction system, and are part of the Pacific Ring of Fire, the ring of volcanoes and associated mountains around the Pacific Ocean.

[10] The Sierra Nevada is an extension of the Cascades toward the south and ends just north of the Transverse Ranges. While the Cascades has a lithology of mainly extrusive Cenozoic volcanic rocks, the Sierra Nevada is mainly intrusive Mesozoic granitic rocks and therefore represents the roots of an ancient volcanic arc. Between the rugged mountains of the California Coastal Ranges and the Sierra Nevada lies the Central Valley (also known as the Great Valley) which is about 650 km long and 80 km wide [*Harden*, 1998]. The valley originated below sea level as an offshore area depressed by subduction of the Farallon Plate into a trench further offshore and was later enclosed by the uplift of the Coast Ranges.

[11] South of the California Coastal Ranges, Central Valley, and the Sierra Nevada lies the east-west trending Transverse Ranges, formed by the convergence of the Pacific and North American plates at the "Big Bend" in the San Andreas Fault [*Humphreys et al.*, 1984; *Humphreys and Hager*, 1990] (Figure 1). Located in southernmost California, the Salton Trough is a pull-apart basin bordered on the northeast by the San Andreas Fault and on the southwest by the San Jacinto Fault. South of the Salton Trough, beyond the

margins of our study, rifting continues down the center of the Gulf of California.

[12] East of the Sierra Nevada is the Basin and Range, extending from eastern California to central Utah, from southernmost Oregon and Idaho to southern Arizona, southwestern New Mexico and further south into the Sonoran State of Mexico. Different causal mechanisms for Basin and Range extension have been proposed including passive and active models. Passive models attribute Basin and Range extension to the stress fields caused by the interaction of North American, Pacific, and Farallon plates: the coupling of the San Andreas Fault and the Queen Charlotte Fault, separated by the Juan de Fuca subduction system, a remnant of the previous Farallon plate [*Christiansen and McKee*, 1978]. Active models attribute the causal mechanism to be (1) the North American plate overriding the East Pacific Rise, (2) back-arc spreading, and (3) the Yellowstone hot spot. East of the Basin and Range is the Colorado Plateau with the Wasatch Front on its north side, and the Rocky Mountain front on its east. The deformation in the Rocky Mountain foreland and continental interior have been attributed to folding of the entire lithosphere as a result of horizontal end load on the western edge of North America during the Laramide compression (75–50 Ma) [*Tikoff and Maxson*, 2001]. Possible causes for the compression are rapid westward drift of the North American Plate and extreme flattening of the Farallon subduction [*Dickinson and Snyder*, 1978]. These features are all marked in Figure 1.

[13] Here we tomographically image the mantle velocity structure beneath these geologic terranes using body waves in an effort to understand their deep structure and origin. Previous surface wave studies show that the average upper mantle S wave velocities of the western United States are considerably slower than that beneath the North American craton [e.g., *van der Lee and Nolet*, 1997; *Marone and Romanowicz*, 2007]. Body wave traveltime tomography studies have better lateral resolution of velocity features in the mantle beneath the western United States due to their more vertical raypath and higher frequencies (0.1 to 10 Hz compared to 0.1 to 0.003 Hz for surface waves) [e.g., *Dueker et al.*, 2001]. They can therefore resolve more detailed velocity features such as the high-velocity Juan de Fuca plate beneath the Cascades, the low-velocity anomalies beneath the Yellowstone and the East Snake River plain, and the high-velocity anomaly beneath the Transverse Ranges of southern California etc.

[14] In this study, we incorporated the Transportable array data with all other available networks resulting in an unprecedented dense distribution of stations in the western Untied States. This allows us to fill the gaps where seismic stations were absent in previous studies, e.g., eastern Oregon, Idaho, central and northern Nevada, northern Utah, and Arizona [e.g., *Rasmussen and Humphreys*, 1988; *Dueker and Humphreys*, 1993; *Bostock and VanDecar*, 1995]. As the distribution of TA stations covers a wider region from the western coastline to eastern boundary of Utah and from the border with Canada in the north to the border with Mexico in the south, it also allows us to image deeper into the mantle revealing new features. In this study we can image to ~1000 km except regions near the edge of the TA array, compared to depths of ~500 km in previous studies when wide TA footprint was not available [e.g., *Rasmussen and Humphreys*, 1988; *Bostock and VanDecar*, 1995]. While previous velocity models derived from body wave traveltime tomographic studies are mostly P wave velocity models, we developed both P and S wave velocity models for the western United States. We refer to our seismic velocity models as DNA07-P for P wave and DNA07-S for S wave, where DNA07 represents the Dynamic North America model of 2007. We chose DNA for the following reasons: (1) the models will provide constraints to the geodynamics of North America; (2) the models will be updated with the progress of the Transportable Array; (3) it is a name easy to remember due to the popularity of its traditional meaning of "deoxyribonucleic acid." This does not imply that the images we obtain are geodynamic images. In short, DNA07-P and DNA07-S are tomographic models showing the P wave and S wave velocity perturbations beneath the western United States from the 1-D global velocity model of IASP91. IASP91 is a standard 1-D average Earth velocity model used as a reference in many seismological studies [*Kennett and Engdahl*, 1991]. The high-resolution DNA07 velocity models of the western United States reveal an extremely heterogeneous mantle structure and provide important clues to mantle convection processes in this tectonically active region and possible interactions between different geological objects, e.g., the subduction of the Juan de Fuca plate and the upwelling of the Yellowstone plume.

## 2. Data and Method

### 2.1. Station Distribution

[15] We use a broadband three component seismic data set collected from the Transportable Array (TA), a component of the National Science Foundation's Earthscope project (www.earthscope.org). The TA includes 400 broadband stations that have been deployed over a near-regular grid of sites with approximately 70 km spacing. The TA will migrate across the United States over the next decade, ultimately occupying about 2000 sites in the conterminous United States and Alaska. The TA data is also complemented by data from 26 other available seismic networks (see full names in Acknowledgments) in the study region as shown in Figure 2. The total number of stations is 809, about half are from the Transportable Array.

[16] Data from all these networks was used in our study. After processing the waveform data and rejecting poor quality waveforms, the total number of stations providing data for the DNA07-S model was 557. For the DNA07-P model 580 stations were used.

### 2.2. Event Distribution

[17] We examined seismic events with epicentral distances greater than 30° and magnitude equal to or greater than 6.0 from 1 January 2006 to 13 October 2007. We expect far fewer useful seismic arrivals for $M < 6$ events due to lower signal-to-noise ratios. We use teleseismic events with epicentral distance $30° \leq \Delta \leq 95°$ as the direct P and S wave arrivals at these distances are relatively simple arrivals. Events with smaller epicentral distances have complex seismograms due to shallow crustal and upper mantle structure. For events from 19 May 2006 to 31 March 2007,

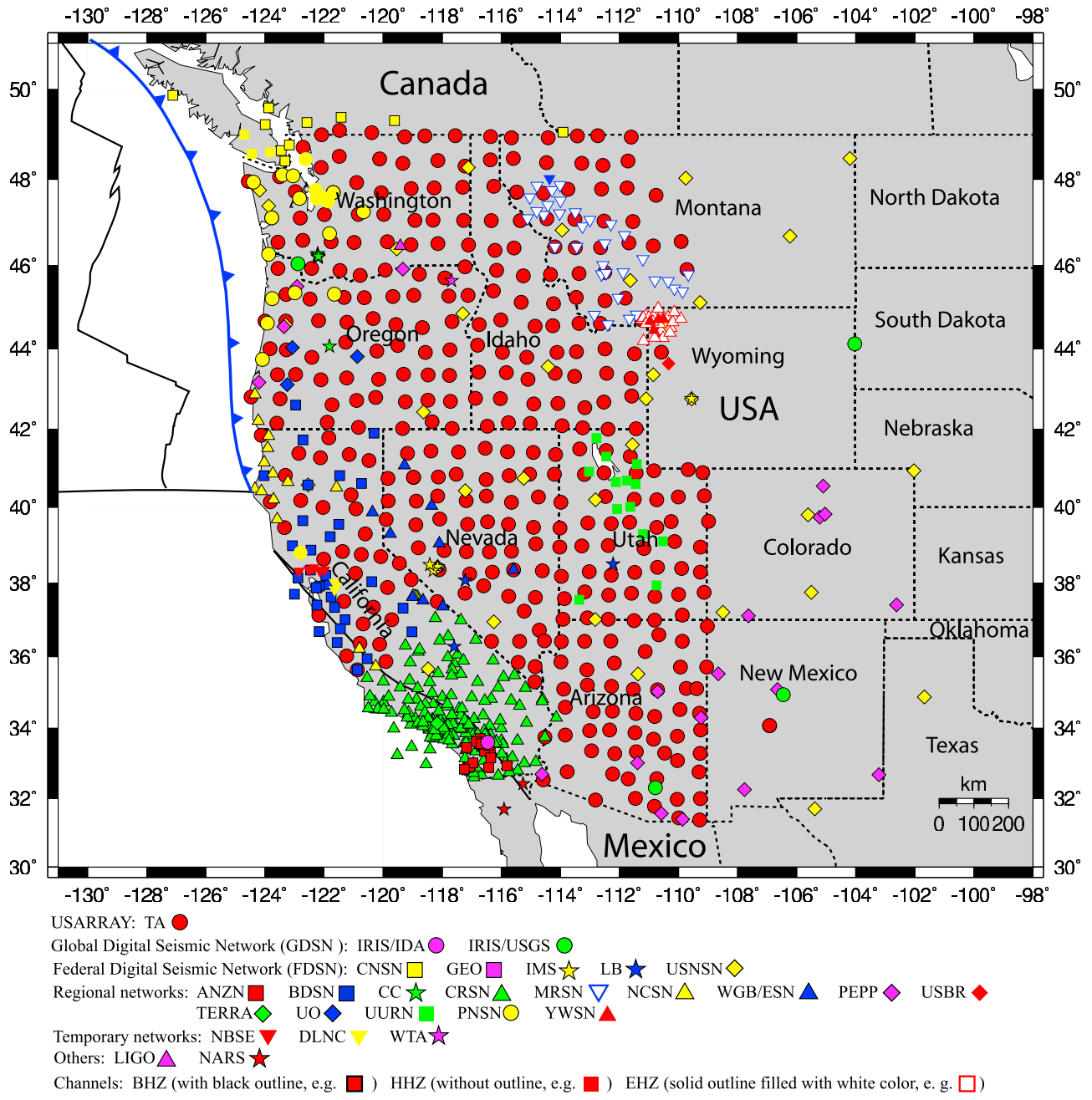


**Figure 2.** The seismic stations used in this study with a total number of 809.

we examined all events at all stations; for events outside this time period, we only examined events which would improve the event back azimuth coverage. In this study, we use direct P and S phase, which have clear arrivals and can be easily identified and core phases when possible.

[18] We use both direct S and SKS phases to build the data set for inverting the DNA07-S model. As direct S phases have higher signal-to-noise ratios on the tangential component than on the radial component, we use arrival data from tangential components for direct S phases. For SKS phases, we use arrival data from radial components. We found 82 events providing useful S picks and 44 events providing useful SKS picks. To build the data set for the DNA07-P model, we examined both direct P phases and core phases and found 75 events providing useful P picks (see Text S1 of the auxiliary materials for more details).[1]

[19] Events are generally clustered in back azimuth from the northwest, west, southwest, and southeast. To reduce the data redundancy, when events are within 1° in epicenter distance as well as back azimuth, we only kept the event which has the highest signal-to-noise ratio and the largest number of picks. We removed 8 redundant events for SKS, 19 events for direct S and P phases.

[20] For the S wave velocity inversion, DNA07-S, a total of 88 events are used with 36 providing clear SKS phases

[1] Auxiliary materials are available in the HTML. doi:10.1029/2008JB006079.

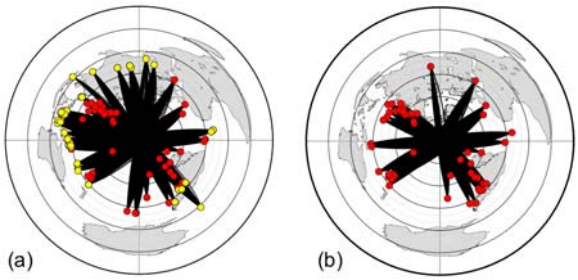


**Figure 3.** Distribution of (a) 88 events and 23,233 rays used in the DNA07-S model inversion and (b) 58 events and 15,141 rays used in the DNA07-P model. The red dots indicate events providing good direct S phases in Figure 3a and P phases in Figure 3b. The yellow dots indicate events providing good SKS phases which are overlaid on the red dots.

and 65 providing clear S phases. These phases are recorded by a total of 557 stations (Figure 3), providing a total of 23,233 rays with 8,371 SKS wave rays and 14,862 S wave rays. For the P wave velocity model, DNA07-P, a total of 58 events are used with clear P phases recorded by 580 stations, resulting in a total of 15,141 rays (Figure 3).

### 2.3. Method

[21] We follow the same inversion procedure as [*Allen et al.*, 2002]. As this approach is a mature technique, we provide only an overview of the technique here. We manually check each waveform for good signal-to-noise ratio and manually pick either the first valley or the first peak. The arrivals are then cross correlated to obtain relative arrival times between all pairs of stations for each event [*Vandecar and Crosson*, 1990]. The average standard deviation of the relative traveltimes determined from cross correlation is 0.014 s for S and 0.005 s for P. The average cross-correlation coefficient is 0.91 for S and 0.89 for P. Rather than reference relative arrival times to an absolute arrival time pick, we set the average relative arrival time of each event to zero. This is equivalent to subtract the mean arrival time at all stations for each event. This approach accommodates timing uncertainties associated with event location, origin time, and eventside earth structures which are common to all raypaths for each event. Traveltime residuals are determined by calculating the relative arrival times at all stations for each event using the 1-D IASP91 global velocity model. The relative traveltime residue for each ray then is obtained by subtracting the predicted values using IASP91 from the observed relative arrival time. Thus the tomographic images we obtained are velocity perturbations from the 1-D reference velocity model of IASP91. This approach has the advantage of eliminating the uncertainties caused by the inaccurate locations of earthquakes as well as our incomplete knowledge about structures outside our study region. The consequence of this approach is the loss of absolute travel time, preventing recovery of velocity anomalies common to all raypaths.

[22] According to the noise analysis of data recorded by the Oregon Array for Teleseismic Study, OATS [*Xue and Allen*, 2007], we expect noise to peak at the frequency range of 0.13–0.3 Hz. To avoid the possible influence of noise, S and SKS arrivals were picked and cross correlated in the frequency window of 0.02–0.1Hz; and P arrivals were processed in the frequency window of 0.8–2.0 Hz. For cross correlation, we chose a window length equal to approximately one wavelength or less for the arrivals observed in each frequency window, which is about 8 s for S and SKS phases and 1 s for P phases.

[23] The dimension of the model space is 5000 × 5000 × 2500 km, with the vertical dimension being 2500 km, and is centered at 40°N and 115°W. The model grid spacing and the smoothing length are 50 km and 100 km, respectively, in all three directions. The region parameterized is more expansive than the volume in which we expect to resolve structure in order to ensure that anomalies are not compressed into the model box.

[24] Our method adopts the high-frequency approximation of ray theory which will underestimate the true amplitude of seismic velocity anomalies by ignoring the Fresnel volume or the Frechet kernels. The width of the Fresnel volume q(x) (the first Fresnel zone) depends on the total distance between the source and receiver, L, the distance from the source, x, and the wavelength, $\lambda$ [*Spetzler and Snieder*, 2004]:

$$q(x) \; < \; 2\sqrt{\frac{\lambda x(L-x)}{L}}\,.$$

The wavelengths of teleseismic P waves used in our study are about 12.5 km given the 1.25 s upper limit of periods and an upper mantle velocity of 10 km/sec. For a raypath length of 10,000 km, the maximum Fresnel width (at the midpoint) is ~350 km. So for the worst scenario, anomalies much smaller than about 350 km wide may not expected to be well resolved in the upper mantle. Actually, as the checkerboard tests (Figures 5 and 6) show that an anomaly with size as small as 250 km can be well resolved at least to 750 km in our study.

### 2.4. Event Corrections and Station Corrections

[25] The mean arrival time differs from event to event depending on the event location and exactly which stations have good arrivals. This causes a baseline shift between the relative traveltime sets for different events. Event corrections were therefore included in the inversion as a set of free parameters to accommodate these baseline shifts and also to account for timing uncertainties associated with event location, origin time, and eventside earth structures, To get more accurate images of the mantle, we also need to correct for crustal effects. There are two approaches to correct and reduce the effect of crustal contamination on the images of the mantle. One approach is to use station corrections where we consider the crustal structure to be unknown. Station corrections correspond to travel time perturbations from a reference model (IASP91 in our case) for the raypaths directly beneath each station. In the inversion, we include a set of free parameters corresponding to station corrections for all stations and invert for them with the goal of removing the crustal traveltime delays from the mantle velocity model. Alternatively a crustal correction could be calculated using existing crustal models to remove a known crustal effect.

[26] There is currently no crustal model covering the study region with a lateral resolution comparable to the station spacing used in this study. Therefore, we use station

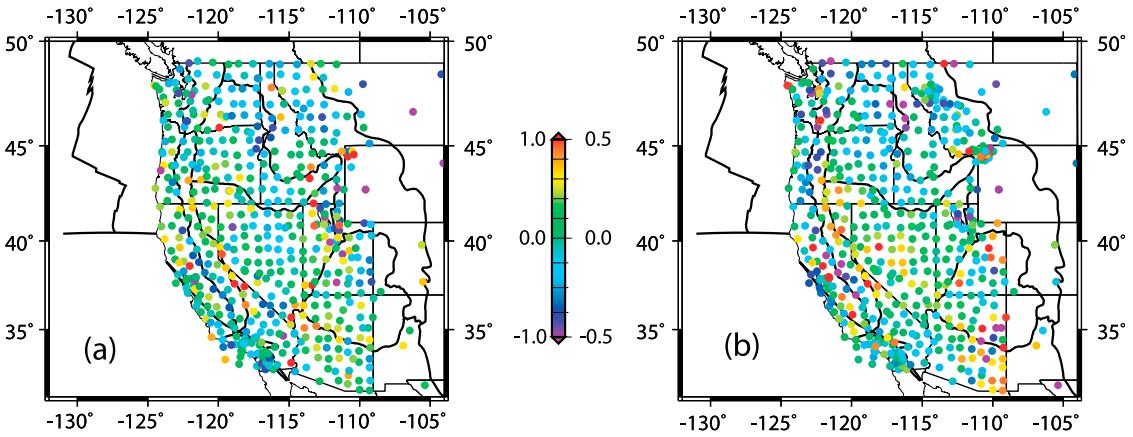


**Figure 4.** Station corrections for (a) the DNA07-S model and (b) DNA07-P model. Units for the color scale are seconds. Labels on the left side of the color scale are for DNA07-S model and those on the right side are for DNA07-P model. Magnitudes of station corrections saturate at 1.0 s and 0.5 s for DNA07-S and -P, respectively, to accentuate more typical corrections. Positive and negative station corrections indicate low- and high-velocity structures present beneath stations, respectively.

corrections in order to correct for the true crustal structure. Rather than leave the station corrections unconstrained in the inversion, we use corrections calculated from an existing crustal model as a reference. We have investigated both CRUST2.0 and EARS (Earthscope Automated Receiver Survey). CRUST2.0 is a global model of crustal structure, topography, and bathymetry with a resolution of 2° [*Bassin et al.*, 2000]. CRUST 2.0 takes advantage of recent compilations of global sediment, ice, and crustal thicknesses which are defined on a 1° × 1° grid and cover most of Eurasia, North America, Australia and some areas of Africa and South America. Sediment thicknesses in each cell are to within 1.0 km of the true sediment thickness and crustal thickness are within 5 km of the true crustal thickness (http://igppweb.ucsd.edu/~gabi/rem.dir/crust/crust2.html). EARS is a crustal model derived from automated receiver function and can be found online at http://www.seis.sc.edu/projects/EARS/index.html [*Crotwell and Owens*, 2005]. The data distribution of EARS is heterogeneous in our study region and its crustal thickness map shows large variations at adjacent stations (Figure S1 in Text S1). We take the approach of solving for station correction in our inversion but use existing crustal models as a guide to the appropriate amplitude of the crustal corrections in a statistical sense. We therefore prefer a smooth crustal model and chose CRUST2.0 as we think it resents a good estimate of the average crustal model in our study region and satisfies our requirement.

[27] Individual ray parameters were used to compute the raypaths and traveltimes through CRUST2.0 using bicubic interpolation and taking into account station elevations. The resulting distribution of CRUST2.0 crustal corrections for the stations used in our study has a standard deviation of 0.50 s for S wave velocity and 0.27 s for P wave velocity. We assume that the distribution of CRUST2.0 crustal corrections represents the distribution of the true crustal corrections and we weight the station corrections in our inversion to have the same standard deviation as the CRUST2.0 correction. This allows us to use CRUST2.0 as a guide to the amplitude of true crustal corrections while letting our data set adjust the individual correction at each station. Figure 4 shows maps of station corrections for the DNA07-S and DNA07-P. We can see that the pattern of station corrections have good correspondence with surface geology. Negative corrections are observed at stations where high-velocity anomalies are expected such as the Cascades, Sierra Nevada, and Wasatch Front. Positive corrections are made at stations where low-velocity anomalies are expected such as Yellowstone, the Basin and Range, and the Central valley. The positive station corrections beneath the Yellowstone are consistent with the observations of low-velocity upper crust beneath Yellowstone [*Stachnik et al.*, 2008].

[28] For the DNA07-S model, a priori standard deviations of 6%, 0.39 s, and 0.32 s were used for the velocity nodes, station corrections, and event corrections, respectively. Similarly, for the DNA07-P model, a priori standard deviations of 3%, 0.28 s, and 0.16 s were used for the velocity nodes, station corrections, and event corrections, respectively. We also include damping in our inversion to push the solution for velocity perturbations toward zero. This is based on the philosophy that we have some idea of what the solution should look like, i.e., the starting model of IASP91, and we don't want to deviate from that unless it is required by the data. The final choice is a tradeoff between damping as little as possible in an effort to increase the fit to the observed data and damping as much as possible to prevent large-amplitude, small-volume, spikes in the velocity model which are most likely due to fitting noise in the data. We have experimented with a range of damping parameters from 0.0 to 1.0. For both the DNA07-S and -P models, a damping factor of 0.1 was used in the inversion. The choice of these parameters affects the apparent velocity structure in the upper ~300 km as traveltime delays are preferentially satisfied by station corrections or velocity anomalies in the uppermost mantle. Different values were tested and variations in these parameters of a factor of 2 or 3 had little effect on the amplitude of structure or velocity anomalies below ~300 km depth.

[29] For the DNA07-S model, the initial RMS residual is 1.83 s and after inversion, the RMS is reduced to 0.49 s, corresponding to a variance reduction of 73%. For the DNA07-P model, after inversion, the RMS residual is

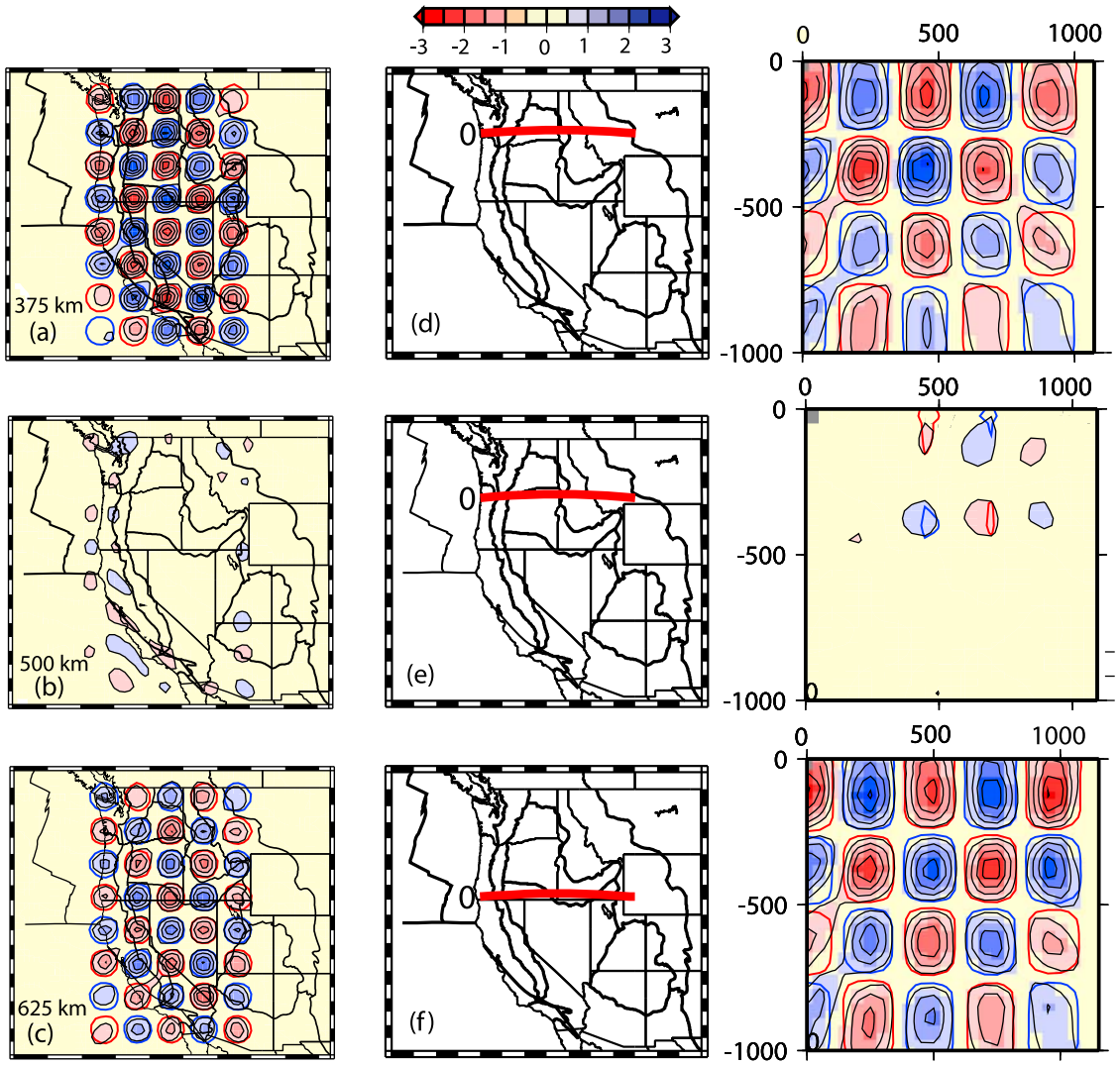


**Figure 5.** Checkerboard test using an input cell size of 250 km for the DNA07-S model. Depth slices of the recovered model are shown at (a) 375 km, (b) 500 km, and (c) 625 km. (d–f) (left) Vertical slices through the recovered model in map view and (right) their corresponding cross sections, with Figure 5d at 46.42°N, Figure 5e at 45.40°N, and Figure 5f at 42.20°N. The amplitude of the input $V_s$ anomaly is 3%. Input models are overlain on the recovered models by thick lines with blue for high input velocity anomalies and red for low-velocity anomalies. The contour interval is 0.5% indicated by vertical lines in the color bar of the velocity scale. Zero contours are not shown.

reduced from the initial 0.60 s to 0.15 s and the var reduction is 74%. The RMS residue was determined using

$$RMS = \sqrt{\frac{1}{N}\sum_{i=1}^{N}(syn_i - data_i)^2},$$

where $syn_i$ indicates the calculated relative traveltime residue using the inverted velocity model, $data_i$ indicates the observed relative travel time residue, and N is the total number of the observed relative travel time residues.

## 3. Checkerboard Resolution Tests

[30] To demonstrate the resolution of our model in general, we conducted several 3-D checkerboard sensitivity tests. A checker board test includes the following steps: (1) build a synthetic velocity model using alternate anomalies of high and low velocities evenly spaced throughout the model horizontally and vertically in a 3-D checkerboard pattern, which is the reason why it's called checker board tests; (2) calculate the predicted relative travel time residues through the synthetic model using the real data geometry; and (3) invert for the velocity model and compare with the synthetic model to assess the ability of the data to resolve the checker board.

[31] First, we conducted a 3-D test with a length scale of 250 km. Each anomaly has the geometry of a cylinder with a vertical axis and a dimension of 250 km in both the vertical and horizontal directions. The amplitude of the synthetic velocity anomaly is 0.135 km/sec for DNA07-S and 0.12 km/sec for DNA07-P. In the vertical direction from the surface to 1000 km depth, we put four layers of alternating

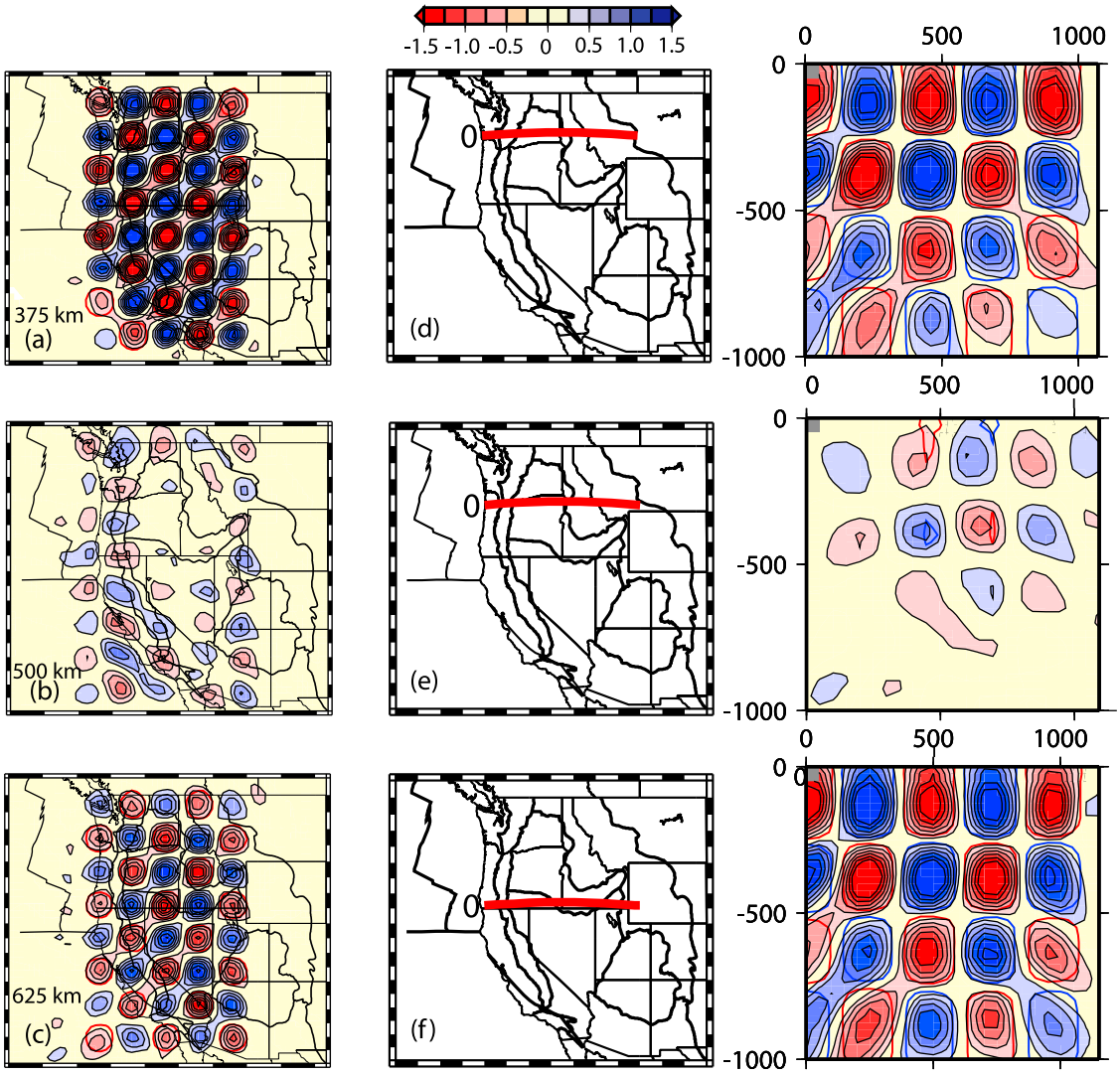


**Figure 6.** Checkerboard test using an input cell size of 250 km for the DNA07-P model. Depth slices and vertical slices of the recovered model are shown at the same depths and cross sections as Figure 5. The amplitude of the input $V_p$ anomaly is 1.5%. Again input models are overlain on the recovered models by thick lines with blue for high-velocity anomalies and red for low-velocity anomalies. The contour interval is 0.25% indicated by vertical lines in the color bar of the velocity scale. Zero contours are not shown.

velocity anomalies which are centered at depths of 125, 375, 625, and 875 km. Figure 5 shows the results for the DNA07-S model. Figures 5a and 5c are two depth slices of the recovered model through the center of two of the input layers, showing the size and shape of the anomalies are recovered very well except along the eastern and southwestern margins of the model where the resolution is reduced as shown on the ray density plots (Figure S4 in text S1). The recovered amplitudes are reduced with increasing depth. Figure 5b is a depth slice through the boundary of two of the input layers, where the velocity anomalies are expected to be zero if no smearing occurs. The little velocity anomalies recovered shows that vertical smearing is insignificant. Figures 5d and 5f are two vertical slices of the recovered model sliced into the center of the input velocity anomalies. They also show that size and shape of the anomalies are well recovered to a depth of 750 km although the recovered amplitudes are reduced at greater depth especially on the east margin. Figure 5e is a vertical slice through the boundary of two of the input columns, showing that horizontal smearing is insignificant. Figure 6 shows the results of the same resolution test for the DNA07-P model. The results demonstrate similar resolution as for the DNA07-S, although there is increased smearing in both the vertical and horizontal smearing directions. This is likely due to the lack of near-vertical core phases in the P model.

[32] The results of the checker board resolution tests show that the percentage of recovery under our inversion scheme is about ~60 to 70% for DNA07-S and ~70% for DNA07-P beneath the array. The recovery is reduced to ~20 to 40% for DNA07-S and 40% for DNA07-P near the margin of the station distribution or at depths greater than 500 km, and

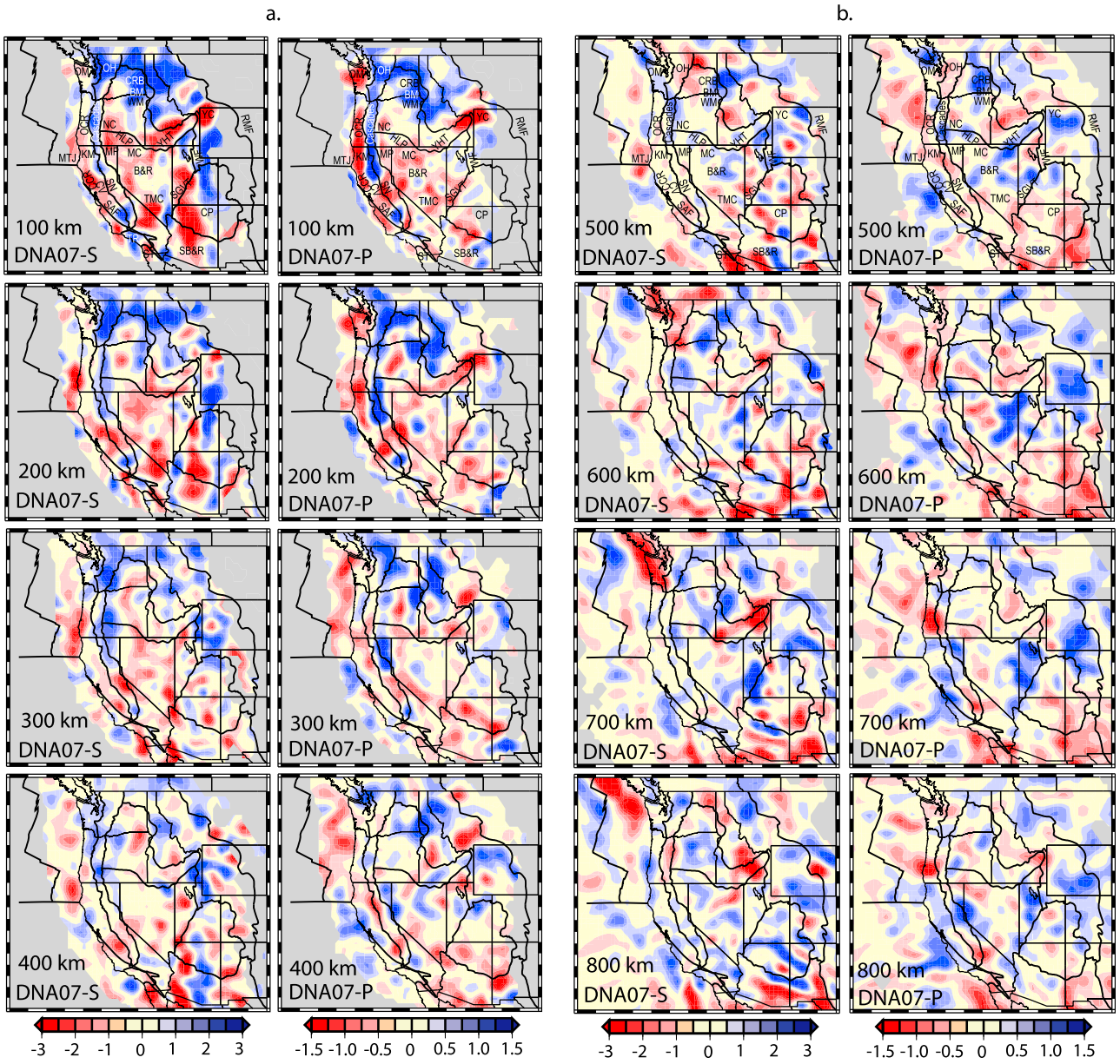


**Figure 7.** (a) Depth slices through the (left) DNA07-S model and (right) DNA07-P model from 100 km to 400 km depth with an interval of 100 km. The corresponding ray density plots are shown in Figure S4 in Text S1. (b) Depth slices through the (left) DNA07-S model and (right) DNA07-P model from 500 km to 800 km depth with an interval of 100 km. The corresponding ray density plots are shown in Figure S4 in Text S1.

especially when both these factors apply. These demonstrate that the observed velocity anomalies in our DNA07 models are likely smaller than the real amplitudes as not all of the anomaly amplitude is recovered during the inversion due to smoothing, damping, and imperfect ray coverage.

[33] As good resolution of small-scale structures does not demonstrate that larger structures can also be retrieved [*Lévêque et al.*, 1993], we conducted 3-D checkerboard tests for larger cell sizes of 500 km and 1000 km. Both tests demonstrate that our data set can retrieve larger structures just as well as the 250 km anomalies. Figures S2 and S3 in Text S1 show the results for 500 km anomalies for DNA07-S and -P, respectively.

[34] In the above synthetic tests and other synthetic tests to follow, we add Gaussian white noise in the synthetic relative traveltime residue. In selecting the amplitude of Gaussian noise, we took the uncertainties of relative travel time residues as references. There are two ways in deciding the standard deviation of noise: (1) use the average standard deviation of relative travel time residues for all rays and (2) use the standard deviation of individual relative travel time residue for each ray which is possible due to the cross-correlation approach. The first approach tends to average out some very large uncertainties for a few rays and results in much smaller peak to peak noise. For example, for the P wave data set, the peak to peak noise is 0.05 s using the

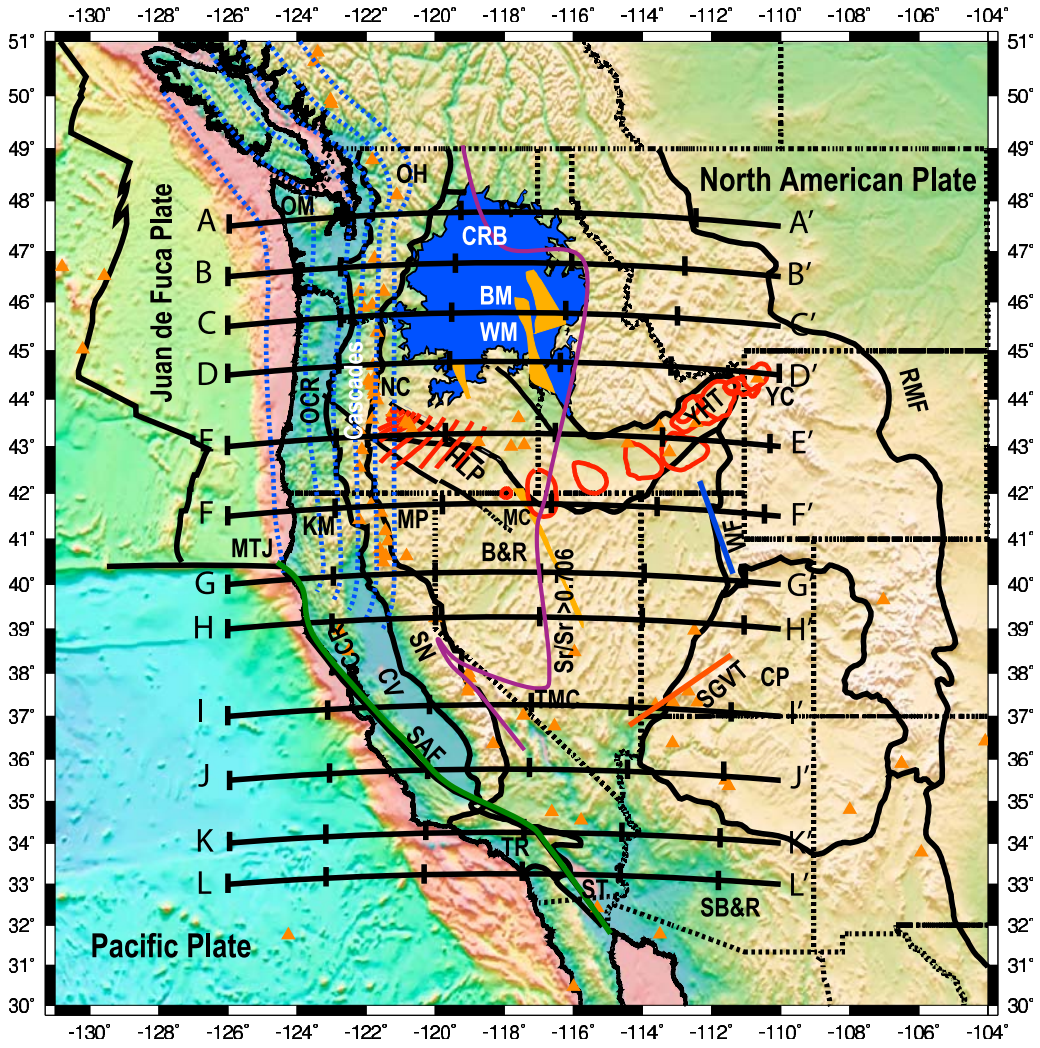


**Figure 8a.** Locations of the vertical cross-section slices shown in Figures 8b–8c and Figure 9.

first approach and is 0.2 s using the second approach. In order to have a better representation of actual noise in data, we used the second approach i.e., the standard deviation of each relative traveltime residue as the reference standard deviation when randomly generating noise for a data point. Our relative travel time residues have a maximum standard deviation of 0.08 s for P wave and 0.3 s for S wave. This results in a peak to peak noise of 0.2 s for the P traveltime data and 0.6 s for the S traveltime data.

## 4. Tomographic Results and Interpretations

[35] Of the two velocity models (P and S velocity), DNA07-S has better event back azimuth coverage, better ray incident angle coverage, and a larger number of events and therefore rays, than DNA07-P (Figure 3). DNA07-S therefore has better resolution as demonstrated in the checkerboard tests (Figures 5 and 6 and Figures S2 and S3 in Text S1). Despite these differences in resolution, the main geologic features in the model region, e.g., the subducted Juan de Fuca plate and the Yellowstone upwelling, are clearly imaged in both models though the detailed geometry sometimes differs. Multiple, regular slices through DNA07-S and -P are shown in Figures 7 and 8. Figure 7 plots depth slices from 100 km depth to 800 km depth with an interval of 100 km, and Figure 8 plots vertical slices corresponding to east-west cross sections from northern Washington to southern California. The main features observed in the DNA07-S and -P models are described in this section. As the features we interpret below are mainly in upper mantle, $V_p$ and $V_s$ depend strongly on temperature and the effect of composition is secondary [*Cammarano et al.*, 2003]. Accordingly, we interpret the observed velocity anomalies in terms of temperature anomalies, i.e., "hot" for low-velocity anomalies and "cold" for high-velocity anomalies. We also use "strong" and "weak" to describe the magnitudes of relative velocity anomalies. In this section, we have corrected for the recovery ability of our inversion scheme, e.g., the recovery percentage is ~60 to 70% for DNA07-S and ~70% for DNA07-P within the model box. Therefore the amplitude of relative velocity anomalies described below reflects their real-Earth amplitudes.

[36] The synthetic tests in section 3 demonstrated that our data set has good resolution and can retrieve features as

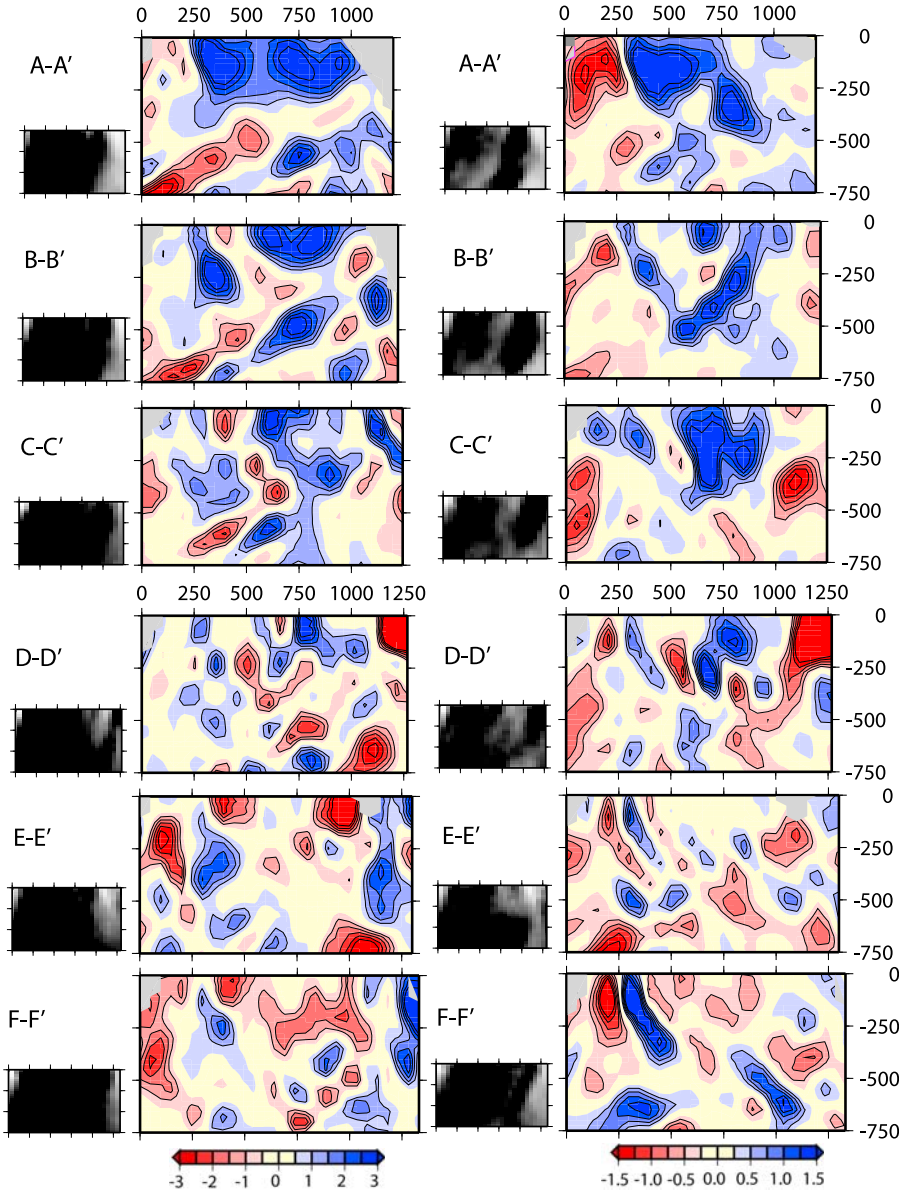


**Figure 8b.** Vertical slices through the (left) DNA07-S and (right) DNA07-P models. The locations of the cross sections are shown in Figure 8a. The color scale is the same as in Figure 7.

larger as 500 to 1000 km across or as small as 250 km across. In addition, we conducted another 3-D checkerboard test with a cell size of 200 km along the same vertical slices as are shown in Figure 8. The results of this test are shown in Figure 9, and helps identification of features from the models (Figure 8) which fall into a region of good resolution and are therefore worthy of interpretation. In addition to the resolution tests, all velocity slices also have a corresponding ray density plot immediately to the left side of the velocity slice. White indicates zero hits and black indicates 100+ hits.

### 4.1. Juan de Fuca Subduction System

[37] The Juan de Fuca subduction system can be observed as a zone of high-velocity anomaly up to 3.6% in DNA07-S and 1.5% in DNA07-P, parallel to the plate margin and beneath the Cascades at 100 km depth which extends toward the east with increasing depth (Figure 7). At 200 km depth, the slab has high-velocity anomalies up to 2.8% in DNA07-S and seems weakened in Oregon with high-velocity anomalies reduced to only 0.25% in DNA07-P. At 300 km depth, the slab is weakened in Oregon and the weakening is more obvious in the DNA07-P model with high-velocity anomalies of up to 0.75%. At 400 km depth, a coherent linear slab pattern is absent in DNA07-S model and the Oregon segment of the slab is absent in DNA07-P model. At greater depths, a coherent slab feature is absent. Note that this region is one of relatively high ray density (Figure S4 in Text S1).

[38] In vertical slices (Figure 8), the slab shows up as a dipping high-velocity anomaly up to 4.3% in DNA07-S and

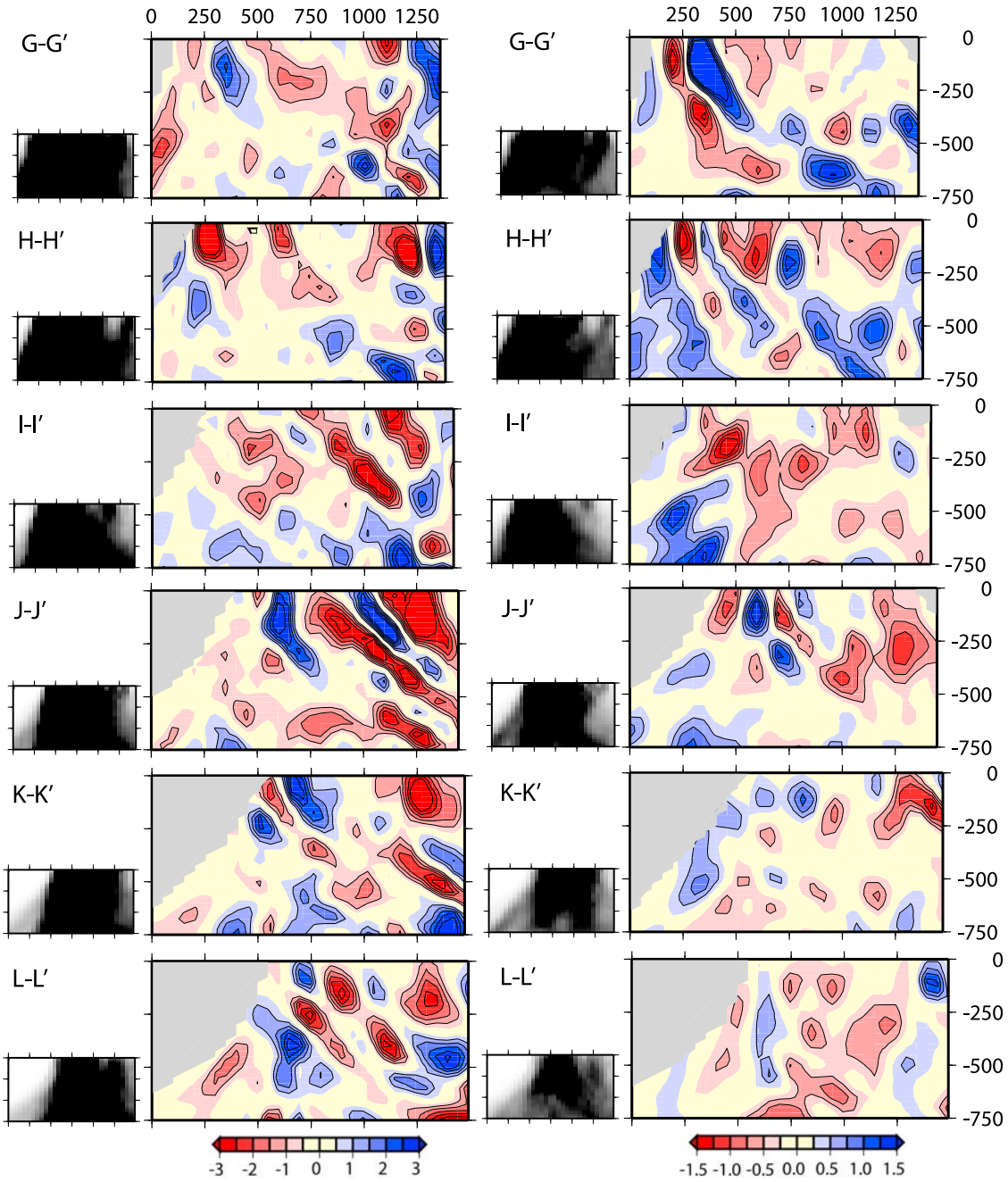


**Figure 8c.** As Figure 8b but for the southern cross sections shown in Figure 8a.

1.8% in DNA07-P reaching 400 km depth in Washington (B-B′), is weakened and disrupted in Oregon (C-C′, D-D′, E-E′), and shows up as a coherent slab feature again beneath northern California (F-F′ and G-G′). An interesting feature is observed in northern California (F-F′) and south of the Mendocino triple junction (G-G′), particularly in DNA07-P, where a dipping high-velocity anomaly is imaged at depths greater than 400 km. This high-velocity anomaly has similar high-velocity perturbations of up to 4.3% in DNA07-S and 2.3% in DNA07-P as the Juan de Fuca slab and is perhaps an old slab fragment from the Cascadia subduction zone. In the disrupted slab section beneath Oregon (C-C′, D-D′, E-E′, particularly in the DNA07-S) the weak slab segment seems to overlay another, deeper slab segment. A tentative explanation is that the deeper slab segment may be a previously broken-off slab which then sank, and continues to sink, due to its negative buoyancy. We also observe a low-velocity zone immediately beneath the Juan de Fuca slab in the DNA07 models from central Oregon to northern California (Figure 8 from E-E′ to G-G′). This zone has a low-velocity anomaly up to ~4.3% in DNA08-S and ~2.3% in DNA08-P and follows the dip of the slab. This low-velocity zone was previously observed in the JdF07 model [*Xue and Allen*, 2007] with an amplitude of ~3% in $V_s$ and interpreted as

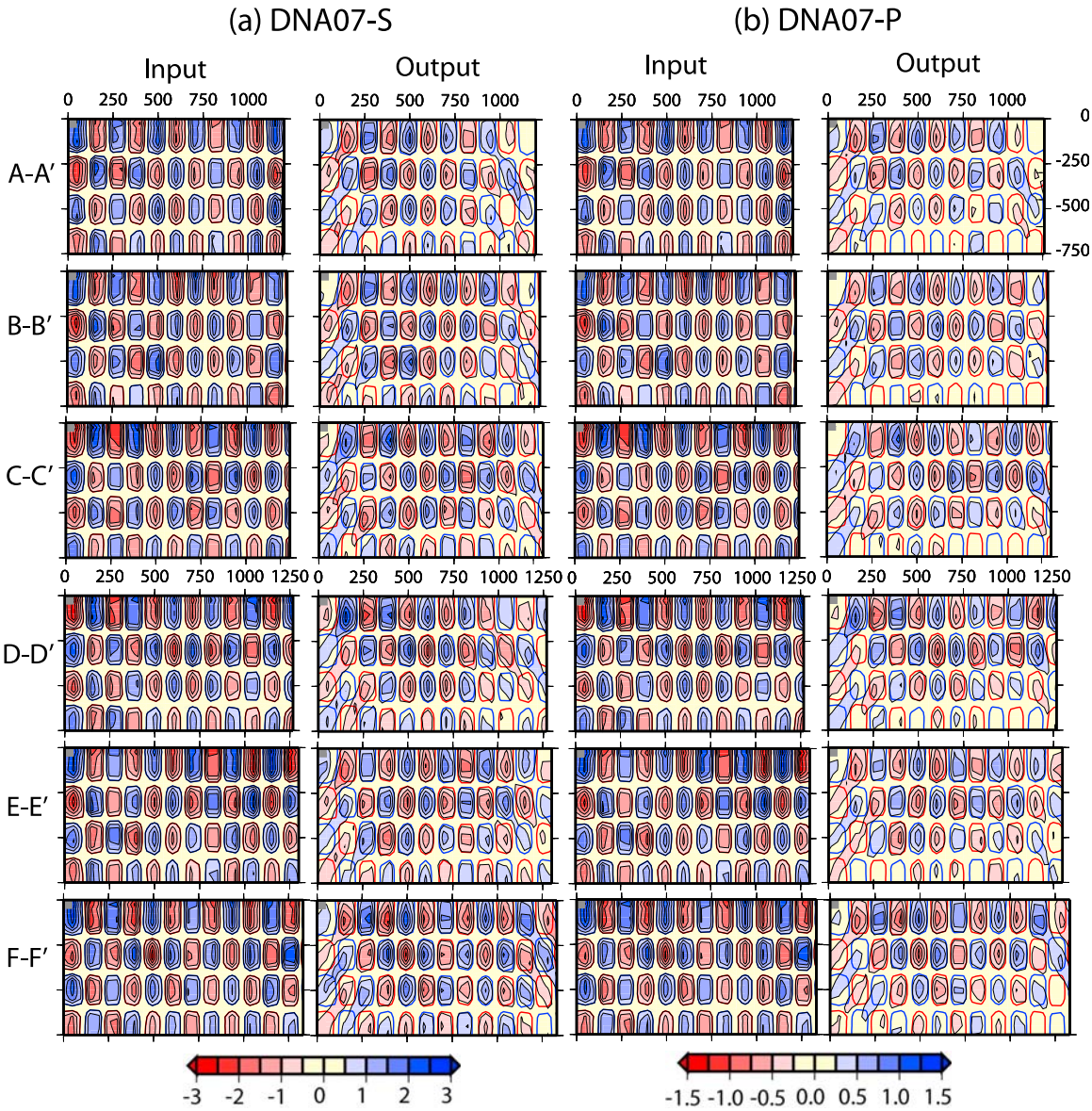


**Figure 9.** (a) Checkerboard test using an input cell size of 200 km for the DNA07-S model. (left) The input model and (right) the output model. The cross sections are taken through the same locations to those in Figure 8. The amplitude of the input is 3% $V_s$. Note as the input amplitudes varies due to being sliced along the great circle instead of a straight line through the same maximum amplitudes, weaker anomalies in the outputs do not necessarily mean worse recoveries. The contour interval and color scale are the same as in Figures 5 and 6. (b) As Figure 9a but for the DNA07-P model and the amplitude of the input is 1.5% $V_p$.

remnant plume head material about 100–300°C hotter than the surrounding mantle which has been dragged down by the Juan de Fuca subducting slab to form the low-velocity zone beneath the slab [*Xue and Allen*, 2007]. Resolution tests in Figures 9 and 10 show that our models have resolution in regions where the above features are imaged.

[39] Previous observations of the slab high-velocity anomalies are ~3.8% for $V_s$ and 1.8% for $V_p$ in Oregon [*Xue and Allen*, 2007]. The slab imaged in this study has a similar high-velocity anomaly up to 3.7% in DNA07-S and 1.8% in DNA07-P in the vertical slice of E-E′ through Oregon. The high-velocity anomalies fall into the range of ~2% to 4% expected for the Juan de Fuca slab [*Xue and Allen*, 2007]. Every 100°C decrease in temperature results in an increase of ~1% in the S wave velocity [*Cammarano et al.*, 2003]. This is consistent with the fact that the temperature anomaly of the Juan de Fuca slab is expected to be between 200 and 400°C colder than the surrounding mantle [*Davies and Stevenson*, 1992] given the slab dip of 60° and subduction rate of 33 mm/yr to 41 mm/yr from northern California to central Washington [*Gripp and Gordon*, 2002].

[40] Previous studies suggest that the slab has a dip of 60° to 65° to the east [*Rasmussen and Humphreys*, 1988; *Bostock and VanDecar*, 1995] or a shallower dip of 45° to the east-northeast [*Michaelson and Weaver*, 1986] beneath northern and central Washington, a dip of 60° to the east beneath

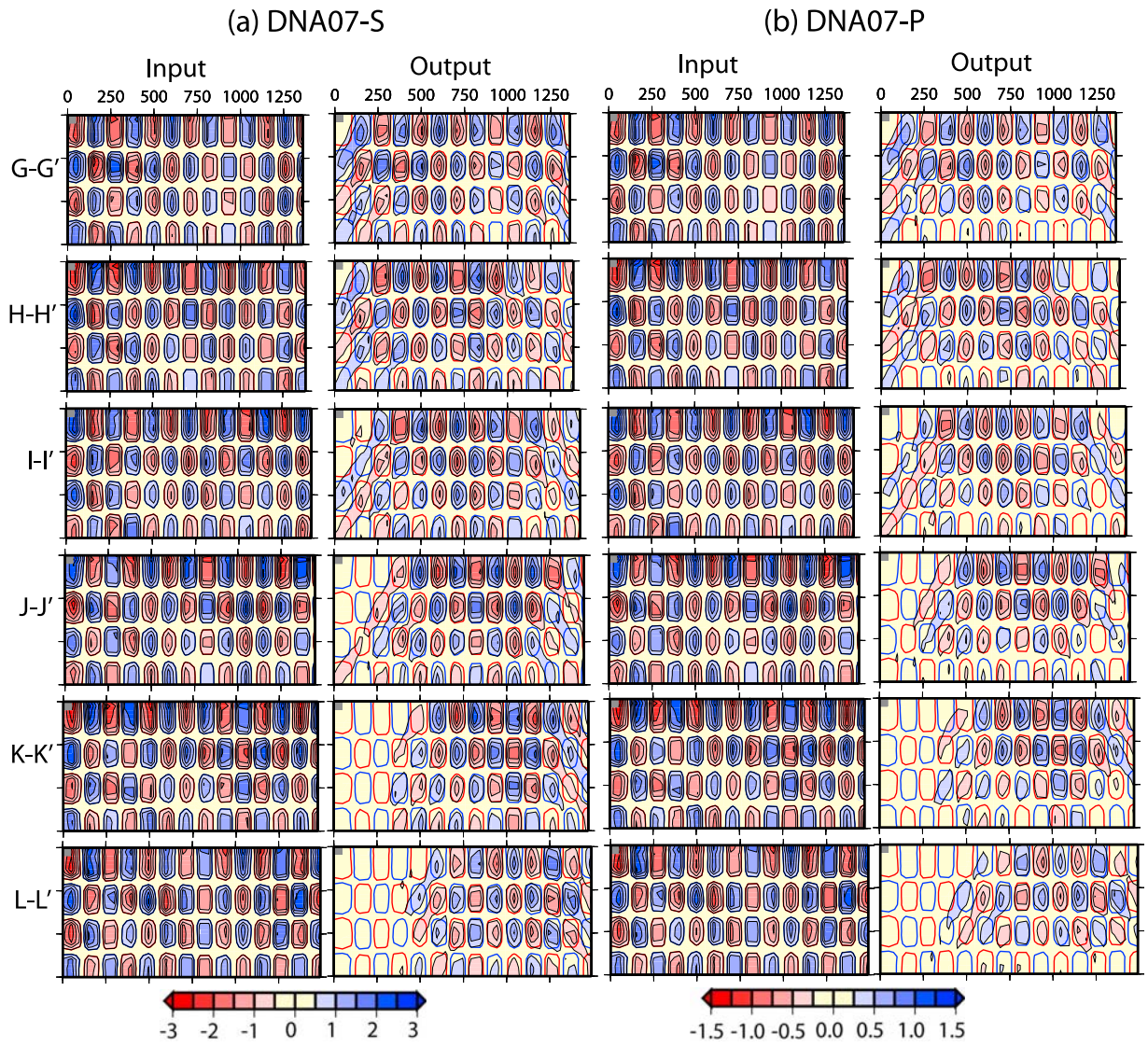


**Figure 9.** (continued)

southern Washington and northern Oregon [*Michaelson and Weaver*, 1986], a dip of 50° [*Xue and Allen*, 2007] or a vertical dip [*Rasmussen and Humphreys*, 1988] beneath the Oregon Cascades, and a dip of ~65° to the east along a NW-SE array across southern Oregon [*Harris et al.*, 1991]. In our DNA07-S model, the dip angle has an average of ~60° and can only be measured in four cross sections in Figure 8: 64° in A-A′, 57° in B-B′, 63° in D-D′, 57° in F-F′. In DNA07-P model, the dip angle has an average of ~58° over seven cross sections from A-A′ to G-G′ in Figure 8: 61° in A-A′, 59° in B-B′ and C-C′, 58° in D-D′ and E-E′, 60° in F-F′, and 53° in G-G′. We can see that there is a difference in the dip between most of the slab to the north of the Mendocino Triple Junction (MTJ) where the dip is nearly a constant of ~60°, and the small fragment to the south of the MTJ (in G-G′) where the dip angle shallows to 53°. This may be due to flow around the southern edge of the slab.

[41] The Juan de Fuca subduction system as described above is in a region away from the edge of the model and we therefore have good resolution as shown in Figure 9. To further illustrate this we conducted velocity anomaly recovery tests on the observed slab feature as shown in Figure 10. This test explores how well our data set can resolve a slab-like anomaly at different depths. We use a synthetic slab anomaly with a dip of 60° to the east below 100 km depth, the average dip imaged in this study. Beneath northern Oregon, *Bostock et al.* [2002] inverted for the S velocity structure of the shallow part of the Cascadia subduction zone using scattered teleseismic waves recorded on an EW oriented portable array and imaged the slab dipping shallowly at ~10° at the western edge of the central Oregon and more steeply of ~30° from the 45 km depth. We therefore us a nearly horizontal synthetic slab above 100 km. We conducted two tests, a synthetic slab ending at 400 km and a slab ending at 600 km (Figure 10). The

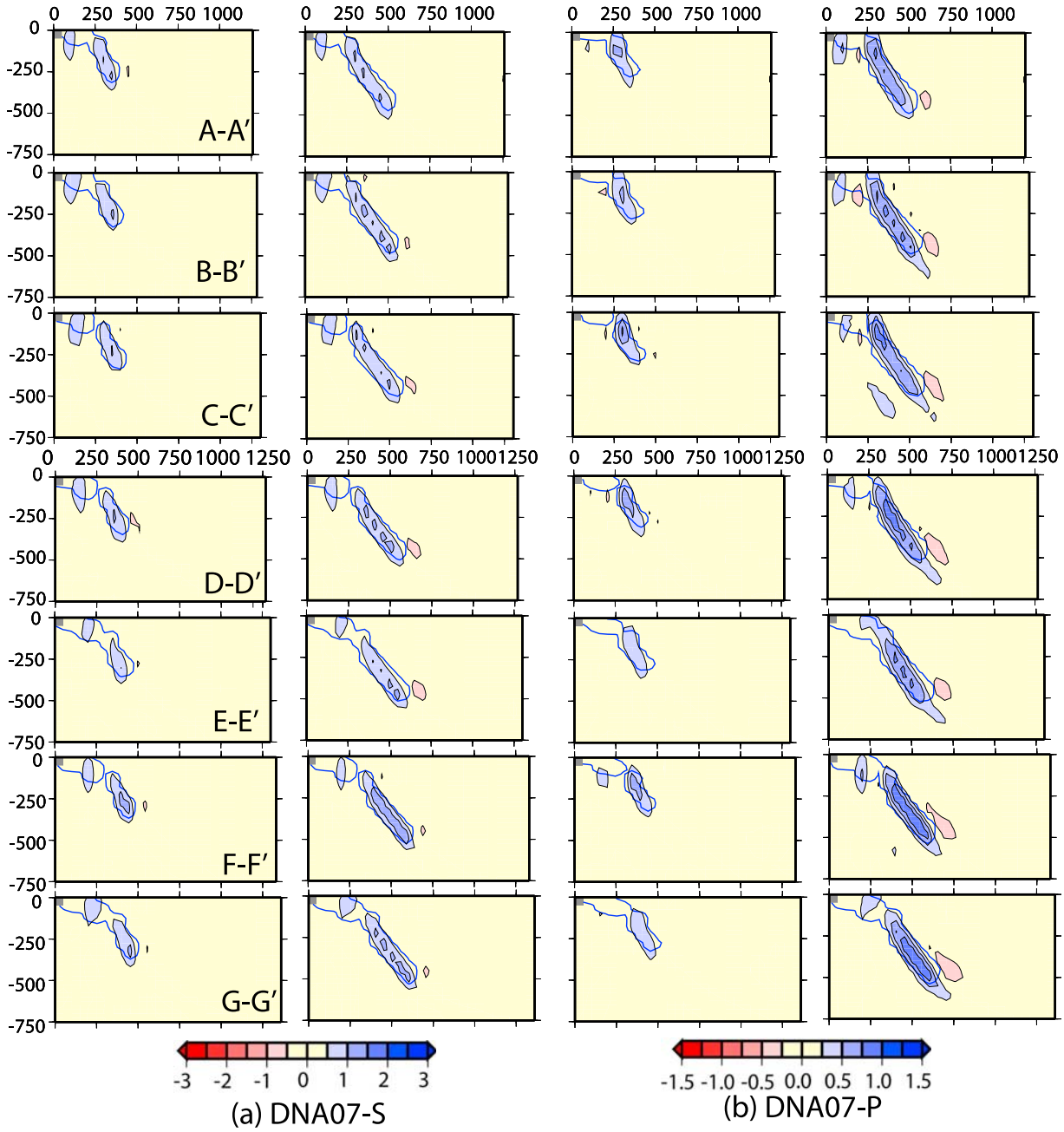


**Figure 10.** Resolution tests on the observed slab feature for (a) the DNA07-S and (b) DNA07-P models. For each model, there are two tests: (left) the recovered model for a synthetic slab ending at 400 km and (right) the recovered model for a synthetic slab ending at 600 km. The cross sections are the same locations as those in Figures 8 and 9. Input models are overlain on the recovered models by thick lines with blue for high-velocity anomaly. The contour interval and color scale are the same as in Figures 5 and 6.

results of the synthetic resolution tests shown in Figure 10 are sliced along the same cross sections as the DNA07-S and -P in Figure 8. The tests show that (1) we can recover the geometry of the slab with insignificant smearing essentially close to zero for the DNA07-S and with minor smearing up to 150 km along the slab for the DNA07-P and (2) slab recovery is very similar in the different cross sections from Washington to northern California. Therefore, the observed disruption of the slab beneath Oregon is most likely real, and the slab, at least in this narrow clearly defined form, stops at about 400 km depth.

[42] The DNA07 observation that the slab stops at 400 km is consistent with the preliminary contention of the JdF07 model [*Xue and Allen*, 2007] and also *Xue and Allen*'s interpretation that the Juan de Fuca subduction system interacted with a Yellowstone plume head around 17 Ma. *Xue and Allen* [2007] calculated the total length of the imaged slab is ~660 km, about 180 km longer than the estimated length of slab subducted since 17 Ma assuming a constant

subduction rate of 28 mm/yr toward the east [*Wilson*, 1988; *Gripp and Gordon*, 1990]. Assuming the same slab geometry 17 Ma as today, this 180 km length of slab would reach ~60 km depth, comparable to the thickness of continental lithosphere. They propose that the absence of the slab below 400 km today is due to the arrival of the Yellowstone plume head ~17 Ma, which destroyed the Juan de Fuca slab at depths greater than the thickness of the continental lithosphere. The additional disruption observed in the slab in Oregon at shallower depths, also imaged by others [*Burdick et al.*, 2008; *Sigloch et al.*, 2008], may indicate that Oregon is the impact location of the Yellowstone plume head with the subducting Juan de Fuca slab. It also explains the absence of deep seismicity in Oregon. Alternatively, *Sigloch et al.* [2008] suggest that the slab hole (what they called "the slab gap") beneath Oregon may be a tear due to slab segments at its two sides subducting at different angles, and further propose that the gap provided an unimpeded ascent for buoyant mantle material to reach the surface and cause the eruption of the Columbia River Basalts. However, this interpretation cannot explain the inclusion of oceanic crust in the melt source for the Columbia River Basalts [*Takahahshi et al.*, 1998].

### 4.2. Yellowstone Upwelling and the Eastern Snake River Plain

[43] In depth slices (Figure 7), DNA07-P shows a strong low-velocity anomaly of more than 2% beneath the Yellowstone region that extends down to 200 km depth. At 300, 400, and 500 km depth, no low-velocity anomaly is observed directly beneath Yellowstone. Instead, a low-velocity anomaly shows up northwest of Yellowstone (Figure 7). This anomaly is much weaker in DNA07-S except at 100 km depth, where a strong low-velocity anomaly is observed directly beneath Yellowstone. At 600 km, a low-velocity anomaly is present in DNA07-S and this feature extends toward the southwest and is still prominent at 800 km depth where it is also observed in DNA07-P. Figure 11a is a NW-SE cross section through the Yellowstone anomaly showing that a strong low-velocity anomaly of more than 4% in DNA07-S and 2% in DNA07-P is located beneath the Yellowstone caldera to a depth of 200 km and then dips toward the northwest. This anomaly stops at 500 km depth and its amplitude is reduced greatly at depths greater than 200 km in DNA07-S with ~3.7% at depths of 250 km and 2.2% around 500 km depth while it remains strong in DNA07-P.

[44] To check whether the dip of the low-velocity anomaly beneath Yellowstone toward the northwest is caused by smearing along rays coming from this back azimuth we conducted a resolution test. In the test, we put a synthetic structure with a low-velocity anomaly of 3% for DNA07-S and 1.5% for DNA07-P beneath the Yellowstone caldera extending down to 250 km, and test whether there is smearing toward the northwest with increasing depth. As shown in Figure 11b, our data set can recover the geometry of this anomaly with little smearing. The amplitude of the recovered anomaly is reduced to 67% for DNA07-S and 33% for DNA07-P,. This demonstrates that the northwest migration of the Yellowstone anomaly with depth is not caused by smearing and most likely a real feature. The observation of such a dipping low-velocity feature is consistent with previous tomographic studies [e.g., *Christiansen et al.*, 2002; *Yuan and Dueker*, 2005; *Waite et al.*, 2006; *Burdick et al.*, 2008].

[45] Along the East Snake River Plain, low-velocity anomalies are observed to 200–250 km depth in both DNA07-S and -P and are flanked by high-velocity anomalies at 100 km (Figure 7, Figure 8 (E-E′), and Figures 11a and 11c). The low-velocity anomaly is a strong and coherent feature from the surface to the depth of ~200 km with an amplitude reaching the 4% for DNA07-S, and 1.5% for DNA07-P. This has been observed before [*Humphreys et al.*, 2000; *Burdick et al.*, 2008] and has been interpreted as partially molten mantle (of low seismic velocity) beneath the hot spot track and basalt-depleted mantle (of high velocity) beneath the rest of the swell [*Humphreys et al.*, 2000]. At much greater depths, greater than 600 km, a strong low-velocity anomaly is clearly visible in DNA07-S and also observed in DNA07-P but with reduced amplitude (Figure 11c). There is no evidence for a low-velocity anomaly connecting this lower mantle feature with the shallow anomaly beneath the Yellowstone caldera. In fact there is a (weak) high-velocity zone separating the shallower (<250 km) and deep (600–1000 km) low-velocity features (Figure 11c). This feature has also been observed by [*Christiansen et al.*, 2002; *Ritsema and Allen*, 2003; *Burdick et al.*, 2008; *Sigloch et al.*, 2008] and been suggested to be the source region of a midmantle plume responsible for the eruption of the Columbia River Basalts [*Sigloch et al.*, 2008].

[46] The suggestion that the present Yellowstone low-velocity anomaly is connected to a deeper mantle source in the transition zone to the northwest of Yellowstone is consistent with the topography of the 410 and 660 mantle discontinuities in this region. The Clapeyron slope for the 410 discontinuity is positive while that for the 660 discontinuity is negative, therefore a vertically coherent thermal anomaly will move the 410 and 660 depths in an opposite direction [*Bina and Helffrich*, 1994]. This anticorrelation of discontinuity topography assumes that thermal effects alone are modulating their depths. *Fee and Dueker* [2004] found that the "410" mantle discontinuity is depressed to a depth of 425 km, 15 km deeper than the normal 410 km depth in a circular region northwest of the Yellowstone caldera which is consistent with higher mantle temperatures in the region as would be expected for a mantle upwelling. However, *Fee and Dueker* [2004] did not find a circular shallowing of the 660 km discontinuity in the same region. Instead, the observed depth of the 660 km discontinuity varies from 655 km to 660 km, suggesting that the same high temperatures are not present at 660km depth. Accordingly, *Fee and Dueker* [2004] argue for the presence of a warm upwelling at the 410 anomaly northwest of the Yellowstone caldera but that the anomaly does not extend across the 660 mantle discontinuity. Our tomographic observations are consistent with this observation.

[47] While we do not image a plume conduit down into the lower mantle, the resolution limit of our model may prevent us from seeing a conduit if the conduit is too narrow. We therefore conducted several tests to determine the resolution limit of our inversion scheme. We put a synthetic low-velocity anomaly beneath the Yellowstone caldera representing a mantle plume. The input anomaly has a radius of 50 km and extends from 0 to 1000 km depth with a −3% velocity perturbation for S and −1.5% for P. Figures 12a

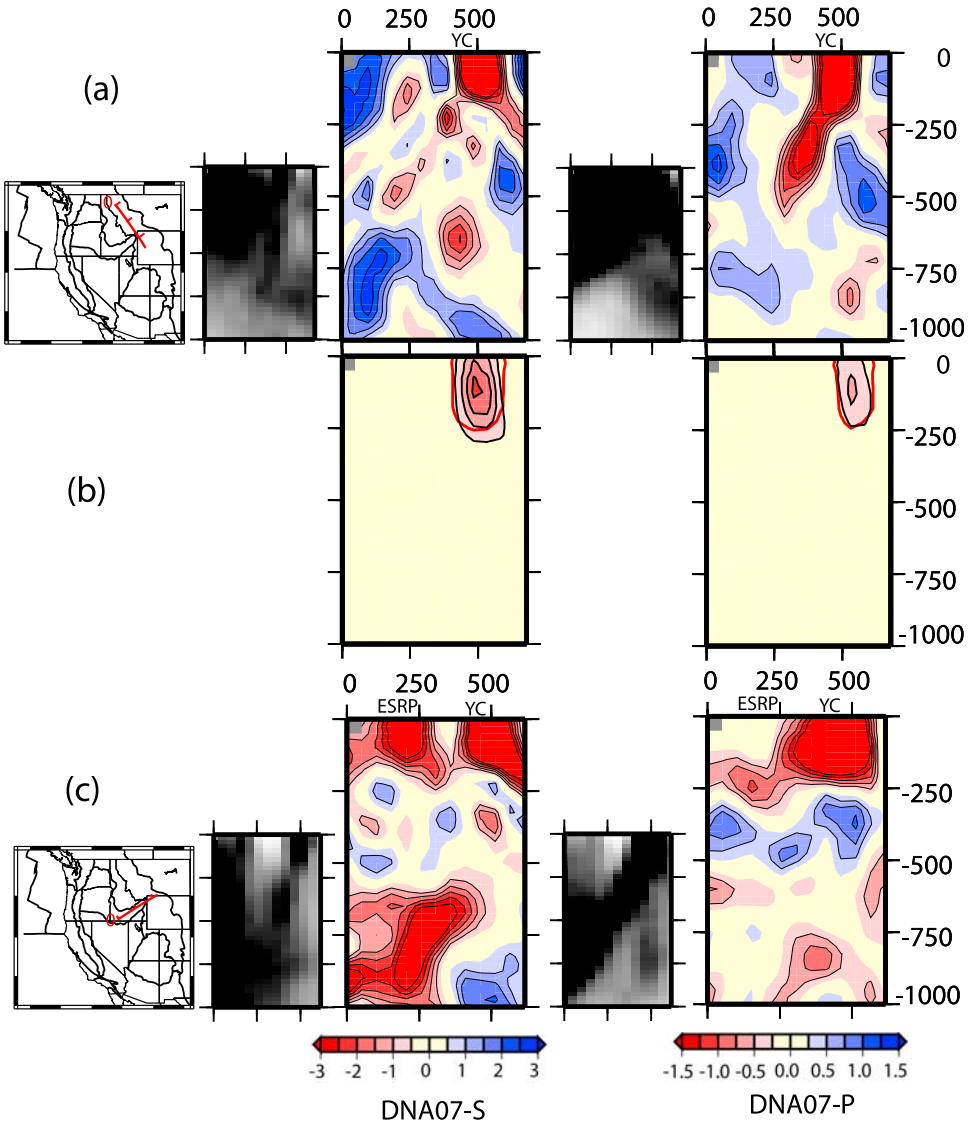


**Figure 11.** Vertical slices through the DNA07 models: (a) a NW-SE cross section through the Yellowstone caldera; (b) the synthetic test along the same cross section as Figure 11a; (c) a cross section along the eastern Snake River Plain.

and 12c show a NW and a SE oriented cross sections through this synthetic plume, respectively, with a maximum low-velocity perturbation of 2.5% for S and 1.25% for P. The corresponding recovered models are shown in Figures 12b and 12d, respectively, and demonstrate that our data set can recover the geometry of the input anomaly but with reduced amplitude at greater depths with a recovery percentage of ~60% at 200 km depth and ~30% at 750 km depth for both S and P. We conducted two additional tests. First, we keep the same −3% and −1.5% velocity perturbations but reduce the conduit radius to 25 km. Second, we use a 50 km radius but reduce the velocity perturbations by 50% to −1.5% and −0.75% for S and P velocity, respectively. In both cases, we are not able to recover the input model (not shown). Thus if the conduit is smaller than 50 km in diameter or the velocity perturbation is small, i.e., less than 1.5% for S velocity and 0.75% for P velocity, our data set will not be able to detect it.

### 4.3. Newberry Track/High Lava Plains

[48] Small-amplitude low-velocity anomalies of ~2.1% in DNA07-S beneath the High Lava Plains and along the Newberry track are observed in the 100 km depth slice but do not extend to the 200 km depth slice (Figure 7). This shallow aspect of the High Lava Plains was also observed by [*Burdick et al.*, 2008]. The vertical cross section of E-E′ in Figure 8 shows the low-velocity anomalies are shallower than 150 km and have no further continuation deeper into mantle. The largest low-velocity anomaly of ~3.6% in DNA07-S and ~0.75% in DNA07-P is directly beneath the Newberry caldera (at ~350 km east from the western end along E-E′, Figure 8) and is offset to the east of the High Cascades volcanic chain. Just as beneath the Yellowstone

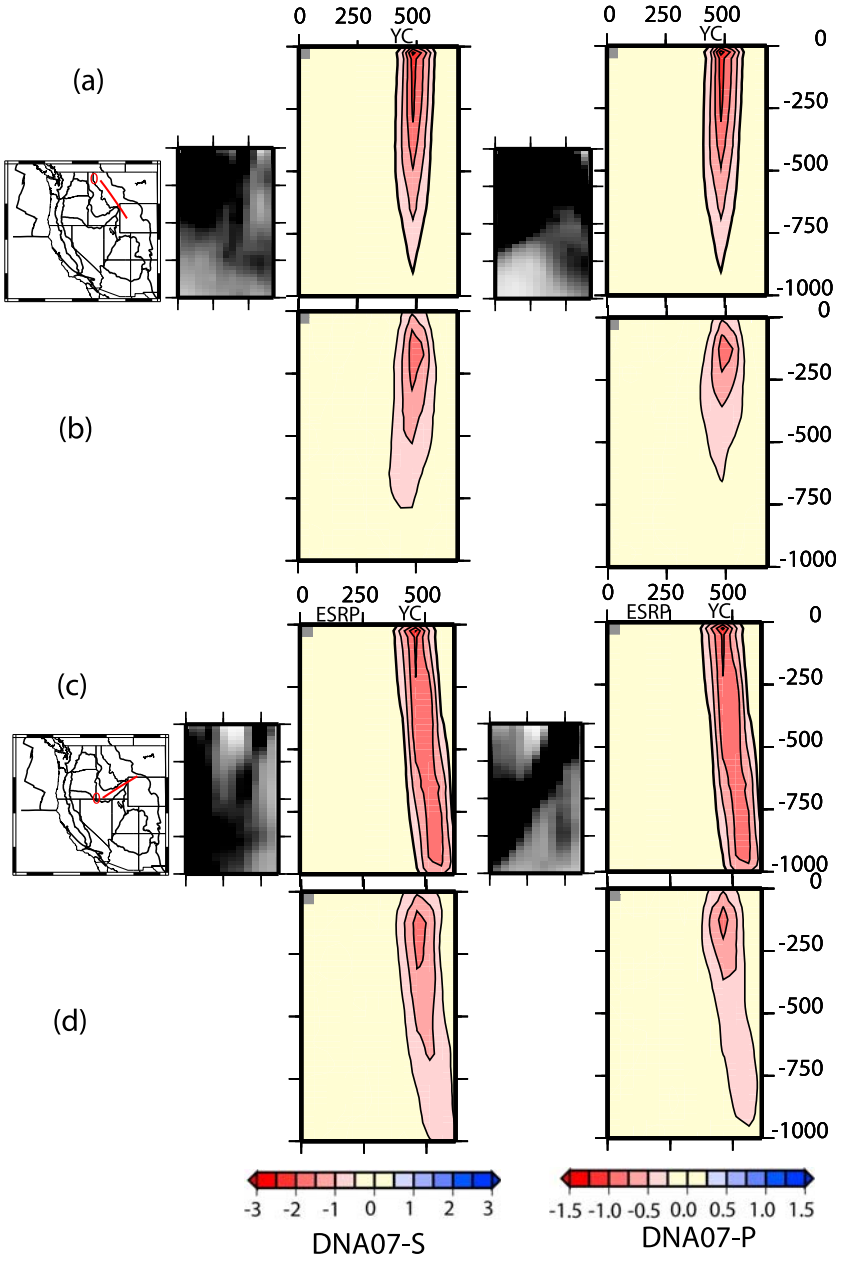


**Figure 12.** A synthetic test for a mantle plume located beneath the Yellowstone caldera. The input anomaly has a radius of 50 km and extends from 0 to 1000 km depth with −3% velocity perturbation in S velocity and −1.5% in P velocity. (a) The same NW-SE cross section as in Figure 11a through the input model and (b) the recovered model; (c) the same cross section along the eastern Snake River Plain as in Figure 11c through the input model and (d) the recovered model.

hot spot track, lower-amplitude low-velocity anomalies are imaged along the track to the northwest (compare Figure 8 E-E′ with Figure 11c, and see the 100 km depth slice of DNA07-S in Figure 7). While shear wave splitting observations suggest flow along the length of the Yellowstone track [e.g., *Waite et al.*, 2005], shear wave splitting results along the Newberry track do not align with flow along the volcanic progression [*Xue and Allen*, 2006]. The seismic anisotropy study led *Xue and Allen* [2006] to conclude that the Newberry hot spot track is not a product of asthenospheric flow, and is more likely a result of lithospheric processes. If this is the case, the low velocities observed in our tomography models may be generated by the melting necessary to generate the volcanism at the surface.

### 4.4. High Velocities Beneath Eastern Washington, Northeastern Oregon and Northern Idaho

[49] A strong high-velocity zone for both DNA07-S and P is observed from 100 to 300 km depth beneath central Washington and extends through northern Idaho reaching

the northwest of Montana (Figure 7). At shallow depths, e.g., 100 km, the high-velocity zone connects with the high-velocity slab (beneath the Cascades at 100 km) and the high-velocity anomaly beneath the northeast Oregon. In the vertical cross section through central Washington (Figure 8 A-A′), this high-velocity zone extends down to 250 to 300 km depth. Beneath northeast Oregon, the Wallowa Mountains, a strong high-velocity anomaly is observed extending to ~400 km depth (Figure 7, Figure 8 C-C′ and D-D′). Similar features were also imaged by *Burdick et al.* [2008].

[50] Previously imaged high-velocity anomalies beneath Washington have been interpreted as thick lithosphere or melt extraction [e.g., *Humphreys and Dueker*, 1994b, and references therein], as the removal of 10% basaltic melt from peridotite would leave a depleted high-velocity residuum behind causing a 1% increase in $V_P$ and more substantial increase in $V_S$ [*Jordan*, 1979]. The location of this high-velocity zone corresponds with the margin of the North American craton as delineated by the $Sr^{87}/Sr^{86}$ > 0.706 line [*Ernst*, 1988] (Figure 1).

[51] *Hales et al.* [2005] imaged a high-velocity anomaly to 175 km depth beneath the Wallowa Mountains. They hypothesized that it is depleted mantle remaining after the eruption of the Columbia River flood basalts which were in turn the result of delamination of the Wallowa plutonic root. This proposes an alternative causal mechanism for the eruption of the Columbia River Basalts, which would not require a mantle plume. Yet, it is still unknown whether this mechanism can explain geochemistry observations such as the elevated $He^3/He^4$ ratios and an inclusion of oceanic crust in the source for the Columbia River Basalts [*Takahahshi et al.*, 1998]. However, plume or no plume, the melt extraction due to the eruption of the Columbia River Basalts can generate high-velocity anomalies in the mantle beneath it and therefore may explain our observed velocity anomalies.

[52] Beneath this broad shallow high-velocity zone, other high-velocity anomalies are observed at greater depths (particularly A-A′ and B-B′ in Figure 8). These are resolved features and illustrate the complexity of upper mantle structure. They may be previously subducted slab segments and/or delaminated craton roots.

### 4.5. High Velocities Beneath Southern Sierra Nevada and Transverse Ranges

[53] A strong high-velocity anomaly >2% in DNA07-P and >4% in DNA07-S is imaged at the southern tip of the Central Valley/Sierra Nevada (Figure 7). In a region of good resolution, this feature shows up with a similar geometry in DNA07-S and -P: from the surface to 200 km depth this anomaly remains nearly vertical and then dips about 45° east ending at 400 km depth east of the southern Sierra Nevada tip (Figure 8 J-J′). This feature, also called "Isabella anomaly" [*Jones et al.*, 1994], has been previously imaged to a depth of 400 km dipping toward east [*Burdick et al.*, 2008], or to a depth of 200 to 300 km [*Biasi and Humphreys*, 1992; *Jones et al.*, 1994; *Saleeby and Ducea*, 2003]. *Biasi and Humphreys* [1992] suggested this anomaly is sinking lithosphere and proposed possible sources of lithospheric material include fragments of slab from Laramide or post-Laramide time or perhaps North American mantle lithosphere removed from neighboring regions [*Biasi and Humphreys*, 1992]. *Jones et al.* [1994] have suggested that this is downwelling lithosphere, which might have started in the Miocene when extensional tectonism deformed San Joaquin Valley and Tehachapi Mountains; this deformation might have introduced an instability in the cold mantle lithosphere beneath the southern Sierra, permitting it to start to move downward. Alternatively, *Saleeby and Ducea* [2003] propose that the subbatholith mantle lithosphere was mechanically delaminated by a shallow segment of the Laramide slab and was replaced by underthrust subduction accretion assemblages.

[54] Beneath the Transverse Ranges a high-velocity anomaly is imaged to a depth of 200 km (Figure 7). This anomaly dips 45° toward the east along the east-west cross section in DNA07-S with an anomaly >4%, but is weaker in DNA07-P with an amplitude of ~1.5% (Figure 8 K-K′). The geometry of the feature beneath the Transverse Ranges is similar to that beneath the southern Sierra Nevada, particularly in DNA07-S (compare Figure 8 J-J′ and K-K′). Similar features have been revealed before in P wave velocity models beneath the Transverse Ranges and been interpreted as downgoing subcrustal lithosphere resulting from the convergence of the Pacific and North American plates [*Humphreys et al.*, 1984; *Humphreys and Hager*, 1990].

[55] In the cross section through this anomaly along the trend of the Transverse Ranges (Figure 13a), a similar velocity structure is observed as that along the K-K′ in Figure 8. In DNA07-S, the high-velocity anomaly is strong and dips 45° toward the east reaching 300 km depth. In addition, a low-velocity zone is imaged with a similar dip of 45° immediately beneath the high-velocity anomaly. In DNA07-P, the high-velocity anomaly is weaker and reaches a depth of 200 km without any apparent dip and there is only a weak low-velocity anomaly beneath. When the anomaly is sliced perpendicular to the trend of the Transverse Ranges (Figure 13b), the high-velocity anomaly has a nearly vertical geometry in both S and P models reaching 200 km depth. A low-velocity zone beneath the high-velocity feature is observed again in the DNA07-S model but absent in the DNA07-P model.

[56] The DNA07 models allow us, for the first time, to image the Transverse Ranges and the southern Sierra Nevada with a similar resolution to the Juan de Fuca subduction system to the north. Compare Figure 8 C-C′ or F-F′ with J-J′ and K-K′, these southern Californian anomalies shows remarkable similarity with the currently subducting slab.

### 4.6. Coastal Ranges

[57] At 100 km depth, a low-velocity zone is located beneath and along the length of the Coastal Ranges from northern Washington to central California. This is particularly clear in DNA07-P where the anomaly is strong everywhere except northern Oregon. The strongest anomalies, in DNA07-P and -S, are beneath the Olympic Mountains and northern California with >2% P and >4% S velocity anomalies (Figure 7). At other locations along this low-velocity zone, velocity anomalies range from 1.4% to 3.6% in DNA07-S but remain high in DNA07-P.

[58] This low-velocity zone can also be observed in the vertical cross sections of A-A′ to H-H′ in Figure 8. The depth

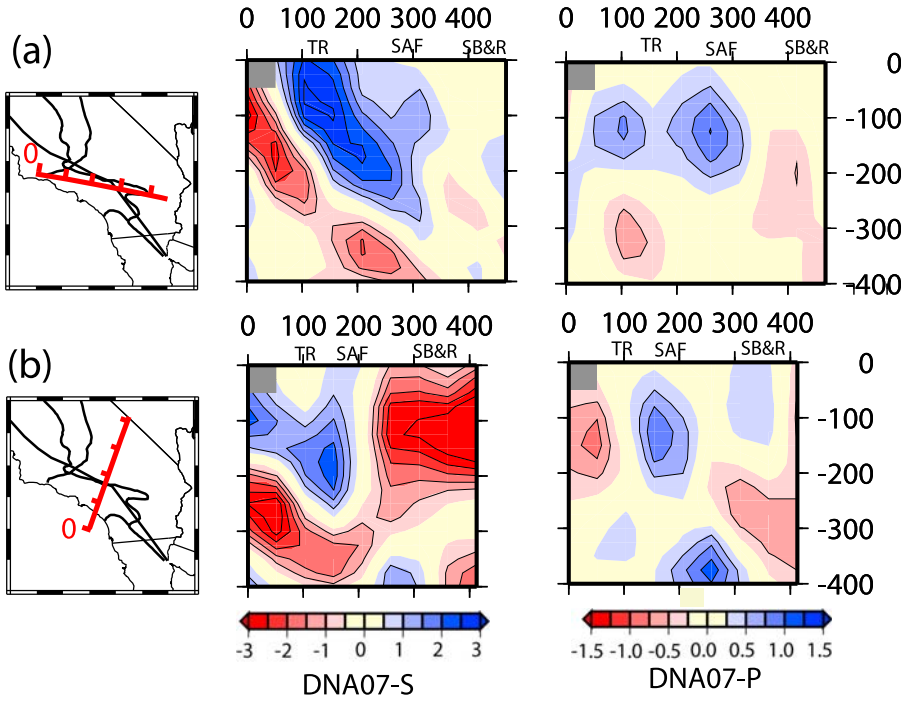


**Figure 13.** Vertical slices through the Transverse Ranges anomaly: (a) an east-west cross section along the trend of the Transverse Ranges; (b) a south-north cross section perpendicular the trend of the Transverse Ranges. The corresponding ray density plots are shown as Figure S5 in Text S1.

it reaches in different cross sections ranges from ~200 km in the north to >500 km in the south. These low-velocity anomalies have also been imaged by *Burdick et al.* [2008]. A possible explanation is that the low-velocity layer has been carried with the oceanic lithosphere from the Juan de Fuca ridge. Low shear velocities have been observed in the upper 200 km offshore west of northern Oregon and Washington near the Juan de Fuca ridge in the global model S20RTS leading to it being categorized as a ridge-type hot spot [*Ritsema and Allen*, 2003].

[59] At the southern end of the anomaly (E-E′ to H-H′) this low-velocity zone lies directly beneath the subducting slab and has a similar dip as the slab. A similar low-velocity feature was observed in JdF07 by *Xue and Allen* [2007] and was interpreted as the remnant plume head material that spread beneath the oceanic lithosphere when the Yellowstone plume head impacted the North American Lithosphere around 17 Ma. The appearance of the feature on cross sections E-E′ through H-H′ is consistent with this interpretation as these east-west sections straddle the latitude of the McDermitt caldera (at 42°N) which is believed to have been the center of the plume head as it is the origin point for the Yellowstone hot spot track.

### 4.7. Low Velocities Above the Juan de Fuca Slab

[60] A strong north-south trending low-velocity zone is observed east of the Cascades from southern Washington to northern Nevada (Figure 7). This low-velocity zone is parallel to the Cascades and extends from the surface down to 300 km depth and has a low-velocity anomaly up to ~3.6% in DNA07-S and ~1.8% in DNA07-P with the maximum velocity perturbation located in central to northern Oregon. In vertical slices (Figure 8), this low-velocity anomaly is located above the subducted slab and can be seen in the cross sections of C-C′, D-D′, E-E′, F-F′, G-G′ and H-H′. This low-velocity anomaly was also present in previous tomographic images [e.g., *Humphreys and Dueker*, 1994b; *Dueker et al.*, 2001; *Burdick et al.*, 2008]. To the south this low-velocity feature merges with the low velocities of the Basin and Range province (F-F′ through H-H′), to the north it is sandwiched between the high velocities of the slab and the Columbia River Basalts.

[61] *Dueker et al.* [2001] interpret the low-velocity anomalies observed at 100 km depth beneath the western U.S. as reflecting the generally thin lithosphere and warm asthenosphere. So far, no specific explanation for these low-velocity anomalies observed above the Juan de Fuca plate in Oregon has been provided. We propose that these anomalies represent remnant plume head material that flowed up along the slab after breaking it up. This caused the low-velocity zone parallel to and east of the Cascades. These are the highest-amplitude low-velocity anomalies observed in Oregon and they are located where the plume interacted with the slab.

### 4.8. "Slab Gap" South of the Mendocino Triple Junction

[62] The "slab gap" was created and has been growing as the Mendocino triple junction migrated north [*Dickinson and Snyder*, 1979]. As the southern edge of the Juan de

Fuca subduction system (i.e., the Gorda plate) migrates north with the triple junction, asthenospheric material emerges and upwells from beneath. We image the slab gap as a low-velocity anomaly up to 3.7% in DNA07-S and 1.8% in DNA07-P extending from the southern end of the Juan de Fuca (including the Gorda) subduction system to latitude of ~37°N just south of the San Francisco Bay region (Figure 7). These low-velocity anomalies are persistent to a depth of ~400 km in both DNA07-S and -P (Figure 7 and Figure 8 H-H′ and I-I′) and have been previously imaged by [*Burdick et al.*, 2008].

[63] The low-velocity anomalies are as expected for a slab gap, where the cold oceanic lithosphere is absent and replaced by the relatively hot asthenosphere, resulting in low-velocity anomalies. These low-velocity anomalies, reaching a depth of ~400 km, suggest that material is upwelling from depths greater that the thickness of the Gorda slab.

### 4.9. Velocity Contrast Across the San Andreas Fault

[64] The San Andreas Fault system delineates strong velocity contrasts between its two sides. At the northern end of the fault, from Cape Mendocino to the San Francisco Bay region, the high-velocity anomalies up to ~2.8% in DNA07-S and ~1.8% in DNA07-P of the Pacific plate are juxtaposed against the low-velocity anomalies >2% in P and >4% in S velocity of the North American plate, as shown in Figure 7 at 100 km depth and G-G′ to I-I′ in Figure 8. The plate boundary in this region is along the coastline so only rays from the west recorded at the coastal stations provide constraints. As the resolution is reduced greatly near the margin, we are not able to give an estimate of the depth extent of the velocity contrast across the plate boundary.

[65] The fault also divides the high velocities at the southern tip of the Central Valley and Sierra Nevada from the low velocities to the southwest of the California Coast Ranges. As to the north, old oceanic lithosphere is adjacent to continental lithosphere at the southern end of the fault but the oceanic material is to the east and the continental material is to the west. The oceanic lithosphere was subducted beneath the Sierra Nevada and the continental material is a slice that has been moved northward by the motion across the San Andreas Fault.

### 4.10. Volcanic Arcs and the Central Valley

[66] Negative station corrections (Figure 4) are observed along the Cascades and Sierra Nevada, indicating the crustal structure is fast which could be due to high velocity or thin crust. The most likely explanation is that these volcanic arcs have cold crystalline roots consisting of the residuals of previous melts. At 100 km depth, fast velocity anomalies are still observed beneath the Cascades in Oregon and northern California, representing the subducted Juan de Fuca plate (Figure 7). However, fast velocity anomalies are not observed beneath the Sierra Nevada at 100 km depth due to the absence of any slab and indicating a shallow origin for the positive station corrections beneath the Sierra Nevada, i.e., a shallow depth for the Sierra Batholith. The negative station corrections of the Sierra Nevada contrast with the positive station corrections for the Central Valley indicating a relatively slow crustal structure likely due to the thick pile of sediments that fills the valley.

### 4.11. Salton Trough

[67] A zone of low velocity is observed under the Salton Trough rift valley, extending to a depth of about 200 km (Figure 7). This zone has a low-velocity anomaly up to 4.3% in DNA07-S and 1.1% in DNA07-P. This is consistent with previous results [*Humphreys et al.*, 1984; *Burdick et al.*, 2008] and the suggestions that small-scale convective upwelling is occurring beneath the rift valley [*Humphreys et al.*, 1984]. The vertical cross section through the Salton Trough anomaly (Figure 8 L-L′) reveals additional low-velocity features extending to greater depths. How these may relate to the rifting processes extending south through the Gulf of California is unclear as this is the southern edge of our model.

### 4.12. Slow Basin and Range and the High-Velocity Anomaly in Central Nevada

[68] Beneath the whole Basin and Range, a low-velocity perturbation is persistent to a depth of ~300 km (Figure 7). In vertical cross sections through the Basin and Range from F-F′ to I-I′ in Figure 8, a coherent low-velocity perturbation is observed extending to ~300 km depth. This anomaly is expected as the whole region is under extension resulting in upwelling of the asthenosphere and a mantle hotter than normal [*Humphreys and Dueker*, 1994a; *van der Lee and Nolet*, 1997]. Different causal mechanisms have been proposed for Basin and Range extension including passive and active models. Passive models attribute Basin and Range extension to the stress fields caused by the interaction of the North American, Pacific, and Farallon plates: the coupling of the San Andreas Fault and the Queen Charlotte Fault, separated by the Juan de Fuca subduction system, a remnant of the previous Farallon plate [*Christiansen and McKee*, 1978]. Active models attribute the causal mechanism to be (1) the North American plate overriding the East Pacific Rise, (2) back-arc spreading, and (3) the Yellowstone hot spot. Base on our observations alone we are not able to discriminate between these models. However, GPS measurements indicate that the Basin and Range is extending at a rate an order of magnitude greater than the Snake River Plain, suggesting that driving forces of Basin and Range extension are beyond those associated with the Yellowstone hot spot [*Lerch et al.*, 2008]. Further, extension directions in the Basin and Range have changed orientation to track the northward migration of the Mendocino Triple Junction. This suggests that the driving forces are realted to stress fields caused by interaction of North American, Pacific, and Farallon plates.

[69] In the center of the Basin and Range low-velocity region we also observe a small high-velocity anomaly beneath central Nevada from 100 km to 300 km depth (Figure 7). This anomaly is stronger in DNA07-P, up to 1.8%, than in DNA07-S with an anomaly of ~0.7%, and can be clearly seen in the vertical H-H′ slice through DNA07-P. While *Burdick et al.* [2008] also imaged a slow Basin and Range to ~300 km, this high-velocity anomaly beneath central Nevada is not seen in their images. This anomaly has also been imaged in other body wave tomographic studies [e.g., *Humphreys and Dueker*, 1994b; *Dueker et al.*, 2001; *West et al.*, 2009] and surface wave studies [*Pollitz*, 2008; *Yang and Ritzwoller*, 2008]. The high-velocity anomaly was

tentatively interpreted as due to melt extraction [*Humphreys and Dueker*, 1994b], or thickened lithosphere [*Dueker and Humphreys*, 1993; *Pollitz*, 2008]. *West et al.* [2009] interpret the anomaly as a downwelling drip of lithosphere. In DNA07-P the shallow (<400 km depth) high-velocity feature connects to a deeper (>400 km depth) high-velocity anomaly to the east (see H-H′, Figure 8). While the resolution degrades below ~500 km depth at this location (see H-H′ in Figure 9), the dip of this feature is parallel to similar dipping features in slices from K-K′ up to F-F′. The slab-like anomaly is continuous from H-H′ up to at least F-F′ and perhaps E-E′ in DNA07-P and while the anomaly is less slab-like, i.e., less continuous, in DNA07-S, high-velocity anomalies are present in the same locations.

### 4.13. Colorado Plateau and the Rocky Mountains

[70] The Colorado Plateau and the Rocky Mountains are located on the eastern edge of our study region and the resolution is therefore reduced. Both DNA07-S and -P image low-velocity anomalies of >2% P and >4% S velocity to depths of 300 to 400 km beneath the northwest and southwest margins of the Colorado Plateau, at the eastern edge of Basin and Range extension (Figure 7).

[71] Beneath the western Rocky Mountains high-velocity anomalies are generally observed with the exception of the Yellowstone region and corresponding low-velocity anomaly (Figure 7 and Figure 8 from A-A′ to F-F′). The contrast across the Wasatch Front is clearly imaged as a transition from the low velocities of the Basin and Range to the high velocities of the Rocky Mountains. We also notice that low-velocity anomalies exist at the 400 km depth slices in the region where *Jasbinsek and Dueker* [2007] found low-velocity layer atop the 410 km discontinuity in the northern Rocky Mountains.

[72] The deformation in the Rocky Mountain foreland and continental interior have been attributed to folding of the entire lithosphere as a result of horizontal end load on the western edge of North America [*Tikoff and Maxson*, 2001]. While we do see high-velocity anomalies beneath the western Rocky Mountains, it is at the eastern margin of our model. The Rocky Mountain Front is beyond the east boundary of our model, as are the Late Cretaceous-Paleogene arches in the foreland region of the Laramide orogeny.

## 5. Implications for Mantle Convection Processes: Origin on Yellowstone and the Fate of the Juan de Fuca Slab

[73] The observation that Juan de Fuca subduction system stops at a depth of 400 km supports the tectonic model proposed by *Xue and Allen* [2007] where the absence of the slab below 400 km depth today is due to the arrival of the Yellowstone plume head around 17 Ma. The plume head would need to break through the slab to reach the base of the North American lithosphere destroying the Juan de Fuca slab at depths greater than the thickness of the continental lithosphere [see *Xue and Allen*, 2007, Figure 4]. Beneath Oregon, the slab is further disrupted at depths <400 km and has a reduced velocity contrast. The slab shallower than 400 km today had not been subducted at 17 Ma. The Oregon disruption to the slab may be due to lingering melting processes in this region which includes the Newberry volcanism. The disruption of the slab in Oregon probably explains the absence of deep seismicity (>30 km) in Oregon, an unusual observation for a subduction zone.

[74] The low-velocity zone immediately beneath the Juan de Fuca slab in southern Oregon and northern California has a similar dip to the slab and was interpreted by *Xue and Allen* [2007] as remnant plume head material being pulled down by the subducting slab after spreading beneath the oceanic lithosphere of the Juan de Fuca plate. An alternative hypothesis is that this material traveled with the Juan de Fuca plate from the Juan de Fuca Ridge. There are also low-velocity anomalies above the slab in this region which may also represent remnant plume head material that reached the surface when the Yellowstone plume head impacted the North American Lithosphere around 17 Ma. Whatever the causal mechanism is, these strong low-velocity anomalies in Oregon correspond to a region where there is an absence of Wadati-Benioff zone earthquakes. Given that the low velocities most likely represent high temperatures, they may be modifying the frictional properties of the interface and be the reason for the absence of seismicity.

[75] While the state of the Juan de Fuca plate can be explained by the proposed history of the Yellowstone plume, beneath Yellowstone we image no vertical whole mantle plume. Instead we only image a strong low-velocity anomaly down to 200 km depth directly beneath Yellowstone. This low-velocity feature then dips toward the northwest but stops at 500 km depth. There is a strong low-velocity region directly beneath Yellowstone at the top of the lower mantle, but there is no evidence for low-velocity conduit connecting this feature to the surface. The resolution limit of our data set prevents us from recovering a conduit smaller than 50 km in diameter or a velocity perturbation less than 1.5% for S velocity and 0.75% for P velocity so a thin weak anomaly may remain undetected.

[76] *Waite et al.* [2006] propose that the low-velocity anomaly dipping to the northwest is the plume conduit. Mantle convection flow models suggest that the conduit could be deformed in the mantle "wind" which could also cause it to segment [*Steinberger*, 2000]. This is their explanation for the fact that the anomaly appears to stop in the transition zone. Another possibility is that the plume was short lived. A significant amount of plume material may have accumulated beneath the slab before breaking through, and today we only see the weak end of the upwelling anomaly. Alternatively there may never have been a mantle plume. However, we prefer the plume model for western North America for several reasons. The plume model is a single process which explains not only Yellowstone and the Yellowstone track, but also our observations of a broken and disrupted Juan de Fuca slab. Our model of slab disruption by a plume is also consistent with the geochemistry. At Yellowstone elevated $^{3}He/^{4}He$ ratios of up to 16 Ra (where 1 Ra = the $^{3}He/^{4}He$ ratio in air) have been observed and is often used to argue for a deep mantle source in the form of a plume [e.g., *Dodson et al.*, 1997], although this is not uncontested [e.g., *Christiansen et al.*, 2002]. In addition, the Columbia River Basalts are mainly aphyric basaltic andesites with a composition that requires a heterogeneous source involving ocean island basaltic material and recycled oceanic crust [*Takahahshi et al.*, 1998]. The suggestion of oceanic crustal material in the source of the Columbia River

Basalts is explained by our model of interaction between the Yellowstone upwelling and the Juan de Fuca subduction system. However, we cannot exclude the possibility that the Yellowstone plume interacted with slabs attached to continental lithosphere and therefore captured signatures of oceanic crust.

[77] Low-velocity anomalies beneath the High Lava Plains and along the Newberry track are observed shallower than 150 km depth and have no further continuation deeper into mantle. This supports the interpretation of an upper mantle origin for the Newberry track [*Xue and Allen*, 2006]. As fast directions from shear wave splitting results do not align with the volcanic progression along the Newberry track, *Xue and Allen* [2006] concluded that the Newberry hot spot track is not a product of asthenospheric flow, and is more likely a result of lithospheric processes. Even if lithospheric faulting is the cause of the Newberry track, the source region for the melts may still include remnant Yellowstone plume head material. The Newberry track itself, therefore, does not argue for or against the Yellowstone plume hypothesis.

[78] As global-scale velocity models typically do not have the resolution to image structures on the scale of those discussed here [e.g., *Bijwaard et al.*, 1998; *Grand*, 2002; *Marone and Romanowics*, 2007], it is difficult to make a direct comparison. *Van der Lee and Nolet* [1997] imaged a high-velocity anomaly above 400 km beneath Cascadia, but they do not image this high-velocity anomaly extending down into the transition zone. This is in contrast to the clear evidence for the Farallon slab in the transition zone to the south of Cascadia where a continuous high-velocity anomaly is observed from northern California to central America. While the resolution in van der Lee and Nolet's model is poorer beneath Cascadia than other parts (van der Lee, personal communication, 2005), their observations are consistent with our interpretation of a hole in the slab. For the Yellowstone region, a northwest slice through the global model S20RTS [*Ritsema and Allen*, 2003] also show a weak low-velocity anomaly beneath the transition zone at Yellowstone [*Christiansen et al.*, 2002].

[79] The imaged heterogeneous structure down to 1000 km depth suggests that the lower mantle may not as homogeneous as we previously thought, and mantle heterogeneity introduced by surface plate tectonics such as subducted slabs may not be constrained to the upper mantle or digested completely in the upper mantle. We find no evidence for separation of a heterogeneous upper mantle from a homogeneous lower mantle. This would support the hypothesis of whole mantle convection.

## 6. Conclusions

[80] Perhaps one of the most striking observations from DNA07-S and -P are just how heterogeneous mantle structure is beneath the western United States. Despite this heterogeneity, there is a very strong correspondence with the complicated tectonics of the region. The main features of the velocity models and their implications are:

[81] North of the Mendocino Triple Junction:

[82] 1. The Juan de Fuca subduction system stops at ~400 km, and is disrupted in Oregon, which we interpret as being due to interaction with the Yellowstone plume head.

[83] 2. West of the Cascades the forearc is imaged as a low-velocity zone beneath the Coastal Ranges with the strongest velocity anomaly beneath the Olympic Mountains and northern California.

[84] 3. East of the Cascades and above the Juan de Fuca slab a north-south trending low-velocity zone is imaged from southern Washington to northern Nevada.

[85] 4. A high-velocity region is imaged from central Washington, through northern Oregon, and into Idaho. Beneath Washington the anomalies reach 250 to 300 km depth and deeper, extending to ~400 km, beneath the Wallowa Mountains of northeast Oregon. These are likely due to a combination of a cold and thick lithosphere and melt extraction during the eruption of the Columbia River Basalts.

[86] 5. The low-velocity anomaly beneath Yellowstone dips toward the northwest and stops at 500 km depth.

[87] 6. A shallow low-velocity zone to ~200 km depth lies beneath the eastern Snake River Plain and does not appear connected to a deeper low-velocity zone at the top of the lower mantle.

[88] 7. We do not detect a low-velocity conduit reaching greater that 500 km depth beneath Yellowstone implying that either (1) any plume was short lived or (2) the conduit is <50 km in diameter and/or the velocity perturbation is less than 1.5% for S and 0.75% for P and therefore unresolved; or (3) there was no deep mantle plume. We prefer the short-lived plume model as it best explains many of the imaged features the Pacific Northwest.

[89] 8. There are only shallow low-velocity anomalies (<150 km depth) along the Newberry hot spot track indicate no deep source.

[90] South of the Mendocino Triple Junction:

[91] 1. In California the high velocities of the Pacific plate are imaged abutting against the low-velocity North American plate.

[92] 2. We image the "slab gap" as low-velocity anomalies extending to 400 km depth from the southern end of the Juan de Fuca subduction system to the southern end of the Sierra Nevada. These anomalies are particularly strong just south of the Mendocino Triple Junction.

[93] 3. High-velocity bodies are imaged beneath the southern tip of the Central Valley/Sierra Nevada and the Transverse Ranges with dips to the east. These may be part of a fossil Farallon subduction system.

[94] 4. The Basin and Range is a region of low velocities to a depth of ~300 km. In the middle of the Basin and Range, in central Nevada, a high-velocity feature is imaged extending to 300 km depth.

[95] 5. A zone of low velocity is observed to 200 km depth under the Salton Trough consistent with ongoing rifting and small-scale convection in the region.

[96] While the upper ~400 km of the DNA07 models correlate well with surface tectonics and geologic provinces, the deeper structure (400–750 km) is equally complex and not easily explained in terms of either existing geologic or geodynamic models. Their further investigation is therefore warranted.

[97] **Acknowledgments.** We thank Ana Luz Acevedo-Cabrera for preprocessing some of the data and Greg Waite for providing crust correction codes. We thank Doug Dreger, Barbara Romanowicz, and Ved Lekic

for beneficial discussions. This work was supported by NSF grants EAR-0643392, EAR-0643077, and EAR-0745934. Mei Xue was partly supported by the State Key Laboratory of Marine Geology, Tongji University. Seismic data for this study was provided by the following networks: Earthscope Transportable Array, Global Seismograph Network (IRIS/IDA and IRIS/USGS), Canadian National Seismograph Network (CNSN), GEOSCOPE (GEO), Leo Brady Network (LB), United States National Seismic Network (USNSN), ANZA Regional Network (ANZA), Berkeley Digital Seismograph Network (BDSN), Cascade Chain Volcano Monitoring (CC), Caltech Regional Seismic Network (CRSN), Montana Regional Seismic Network (MRSN), Northern California Seismic Network (NCSN), Western Great Basin/Eastern Sierra Nevada (WGB/ESN), Princeton Earth Physics Project-Indiana (PEPP), U.S. Bureau of Reclamation Seismic Networks (USBR), Southern California Seismic Network TERRAscope (TERRA), University of Oregon Regional Network (UO), University of Utah Regional Network (UURN), Pacific Northwest Regional Seismic Network (PNSN), Yellowstone Wyoming Seismic Network (YWSN), North Bay Seismic Experiment (NBSE), DELTA LEVY Northern California (DLNC), Wallowa TA 2006–2008 (WTA), Laser Interferometer Gravitational-Wave Experiment (LIGO), and the Network of Autonomously Recording Seismographs (NARS). Most of these data were made available by the IRIS DMC. The figures were generated using GMT [*Wessel and Smith*, 1995]. This is Berkeley Seismological Laboratory contribution 08–09.

## References

Allen, R. M., et al. (2002), Imaging the mantle beneath Iceland using integrated seismological techniques, *J. Geophys. Res.*, *107*(B12), 2325, doi:10.1029/2001JB000595.

Anders, M. H., J. W. Geissman, L. A. Piety, and J. T. Sullivan (1989), Parabolic distribution of circumeastern Snake River Plain seismicity and latest Quaternary faulting, migratory pattern and association with the Yellowstone hotspot, *J. Geophys. Res.*, *94*, 1589–1621, doi:10.1029/JB094iB02p01589.

Anderson, D. L. (1998), The helium paradoxes, *Proc. Natl. Acad. Sci. U. S. A.*, *95*, 4822–4827, doi:10.1073/pnas.95.9.4822.

Bassin, C., G. Laske, and G. Maters (2000), The current limits of resolution for surface wave tomography in North America, *Eos Trans. AGU*, *81*, F897.

Biasi, G. P., and E. D. Humphreys (1992), P-Wave Image of the upper mantle structure of central California and southern Nevada, *Geophys. Res. Lett.*, *19*, 1161–1164, doi:10.1029/92GL00439.

Bijwaard, H., W. Spakman, and E. R. Engdahl (1998), Closing the gap between regional and global travel time tomography, *J. Geophys. Res.*, *103*, 30,055–30,078.

Bina, C. R., and G. Helffrich (1994), Phase-transition clapeyron slopes and transition zone seismic discontinuity topography, *J. Geophys. Res.*, *99*, 15,853–15,860, doi:10.1029/94JB00462.

Blackwell, D. D. (1969), Heat-flow determinations in the northwestern United States, *J. Geophys. Res.*, *74*, 992–1007, doi:10.1029/JB074i004p00992.

Bostock, M. G., and J. C. VanDecar (1995), Upper-mantle structure of the northern Cascadia subduction zone, *Can. J. Earth Sci.*, *32*, 1–12.

Bostock, M. G., R. D. Hyndman, S. Rondenay, and S. M. Peacock (2002), An inverted continental Moho and serpentinization of the forearc mantle, *Nature*, *417*, 536–538, doi:10.1038/417536a.

Burdick, S., C. Li, V. Martynov, T. Cox, J. Eakins, T. Mulder, L. Astiz, F. L. Vernon, G. L. Pavlis, and R. D. van der Hilst (2008), Upper mantle heterogeneity beneath north America from travel time tomography with global and USArray transportable array data, *Seismol. Res. Lett.*, *79*, 384–392, doi:10.1785/gssrl.79.3.384.

Cammarano, F., S. Goes, P. Vacher, and D. Giardini (2003), Inferring upper-mantle temperatures from seismic velocities, *Phys. Earth Planet. Inter.*, *138*, 197–222, doi:10.1016/S0031-9201(03)00156-0.

Camp, V. E., and B. B. Hanan (2008), A plume-triggered delamination origin for the Columbia River basalt group, *Geosphere*, *4*, 480–495, doi:10.1130/GES00175.1.

Chesley, J. T., and J. Ruiz (1998), Crust-mantle interaction in large igneous provinces: Implications from the Re-Os isotope systematics of the Columbia River flood basalts, *Earth Planet. Sci. Lett.*, *154*, 1–11, doi:10.1016/S0012-821X(97)00176-3.

Christiansen, R. L., and E. H. McKee (1978), Late Cenozoic volcanic and tectonic evolution of the Great Basin and the Columbia intermontane regions, in *Cenozoic Tectonics and Regional Geophysics of the Western Cordillera*, edited by R. B. Smith and G. P. Eaton, *Mem. Geol. Soc. Am.*, *152*, 283–311.

Christiansen, R. L., G. R. Foulger, and J. R. Evans (2002), Upper-mantle origin of the Yellowstone hotspot, *Geol. Soc. Am. Bull.*, *114*, 1245–1256, doi:10.1130/0016-7606(2002)114<1245:UMOOTY>2.0.CO;2.

Craig, H., J. E. Lupton, J. A. Welhan, and R. Poreda (1978), Helium isotope ratios in Yellowstone and Lassen Park volcanic gases, *Geophys. Res. Lett.*, *5*, 897–900, doi:10.1029/GL005i011p00897.

Crotwell, H. P., and T. J. Owens (2005), Automated receiver function processing, *Seismol. Res. Lett.*, *76*, 702–709.

Davies, J. H., and D. J. Stevenson (1992), Physical model of source region of Subduction Zone volcanics, *J. Geophys. Res.*, *97*, 2037–2070, doi:10.1029/91JB02571.

Dickinson, W. R., and W. S. Snyder (1978), Laramide folding associated with basement block faulting in the western United States, in *Plate Tectonics of the Laramide Orogeny*, edited by V. Matthews, *Mem. Geol. Soc. Am.*, *151*, 355–366.

Dickinson, W. R., and W. S. Snyder (1979), Geometry of triple junctions related to San Andreas transform, *J. Geophys. Res.*, *84*, 561–572, doi:10.1029/JB084iB02p00561.

Dodson, A., B. M. Kennedy, and D. J. DePaolo (1997), Helium and neon isotopes in the Imnaha Basalt, Columbia River Basalt Group: Evidence for a Yellowstone plume source, *Earth Planet. Sci. Lett.*, *150*, 443–451, doi:10.1016/S0012-821X(97)00090-3.

Draper, D. S. (1991), Late Cenozoic bimodal magmatism in the northern basin and range province of southeastern Oregon, *J. Volcanol. Geotherm. Res.*, *47*, 299–328, doi:10.1016/0377-0273(91)90006-L.

Dueker, K. G., and E. D. Humphreys (1993), Teleseismic imaging of the western United States upper mantle structure using the Simultaneous Iterative Reconstruction Technique, in Seismic Tomography: Theory and Practice, edited by H. M. Iyer and K. Hirahara, pp. 265–298, Blackwell, London.

Dueker, K., H. Yuan, and B. Zurek (2001), Thick-structured Proterozoic lithosphere of the Rocky Mountain region, *GSA Today*, *11*, 4–9, doi:10.1130/1052-5173(2001)011<0004:TSPLOT>2.0.CO;2.

Ernst, W. G. (1988), Metamorphic terranes, isotopic provinces, and implications for crustal growth of the Western United States, *J. Geophys. Res.*, *93*, 7634–7642, doi:10.1029/JB093iB07p07634.

Fee, D., and K. Dueker (2004), Mantle transition zone topography and structure beneath the Yellowstone hotspot, *Geophys. Res. Lett. 31*, L18603, doi:10.1029/2004GL020636.

Fournier, R. O. (1989), Geochemistry and dynamics of the Yellowstone National Park hydrothermal system, *Annu. Rev. Earth Planet. Sci.*, *17*, 13–53, doi:10.1146/annurev.ea.17.050189.000305.

Geist, D., and M. Richards (1993), Origin of the Columbia Plateau and Snake River Plain: Deflection of the Yellowstone Plume, *Geology*, *21*, 789–792, doi:10.1130/0091-7613(1993)021<0789:OOTCPA>2.3.CO;2.

Grand, S. P. (2002), Mantle shear-wave tomography and the fate of subducted slabs, *Philos. Trans. R. Soc. A*, *360*, 2475–2491.

Gripp, A. E., and R. G. Gordon (1990), Current plate velocities relative to the hotspots incorporating the NUVEL-1 global plate motion model, *Geophys. Res. Lett.*, *17*, 1109–1112, doi:10.1029/GL017i008p01109.

Gripp, A. E., and R. G. Gordon (2002), Young tracks of hotspots and current plate velocities, *Geophys. J. Int.*, *150*, 321–361, doi:10.1046/j.1365-246X.2002.01627.x.

Hales, T. C., D. L. Abt, E. D. Humphreys, and J. J. Roering (2005), A lithospheric instability origin for Columbia River flood basalts and Wallowa Mountains uplift in northeast Oregon, *Nature*, *438*, 842–845, doi:10.1038/nature04313.

Harden, D. R. (1998), *California Geology*, 479 pp., Prentice Hall, Upper Saddle River, N. J.

Harris, R. A., H. M. Iyer, and P. B. Dawson (1991), Imaging the Juan de Fuca plate beneath southern Oregon using teleseismic P-Wave residuals, *J. Geophys. Res.*, *96*, 19,879–19,889, doi:10.1029/91JB02046.

Hill, R. I., I. H. Campbell, G. F. Davies, and R. W. Griffiths (1992), Mantle plumes and continental tectonics, *Science*, *256*, 186–193, doi:10.1126/science.256.5054.186.

Humphreys, E. D., and K. G. Dueker (1994a), Physical state of the western U.S. upper mantle, *J. Geophys. Res.*, *99*, 9635–9650, doi:10.1029/93JB02640.

Humphreys, E. D., and K. G. Dueker (1994b), Western U.S. upper mantle structure, *J. Geophys. Res.*, *99*, 9615–9634, doi:10.1029/93JB01724.

Humphreys, E. D., and B. H. Hager (1990), A kinematic model for the Late Cenozoic development of southern California crust and upper mantle, *J. Geophys. Res.*, *95*, 19,747–19,762, doi:10.1029/JB095iB12p19747.

Humphreys, E., R. W. Clayton, and B. H. Hager (1984), A tomographic image of mantle structure beneath Southern California, *Geophys. Res. Lett.*, *11*, 625–627, doi:10.1029/GL011i007p00625.

Humphreys, E. D., K. G. Dueker, D. L. Schutt, and R. B. Smith (2000), Beneath Yellowstone: Evaluating plume and nonplume models using teleseismic images of the upper mantle, *GSA Today*, *10*, 1–7.

Jasbinsek, J., and K. Dueker (2007), Ubiquitious evidence for a low velocity layer atop the 410 km discontinuity, *Geochem. Geophys. Geosyst.*, *8*, Q10004, doi:10.1029/2007GC001661.

Jones, C. H., H. Kanamori, and S. W. Roecker (1994), Missing roots and mantle "drips": Regional $P_n$ and teleseismic arrival times in the southern Sierra Nevada and vicinity, California, *J. Geophys. Res.*, *99*, 4567–4601, doi:10.1029/93JB01232.

Jordan, B. T. (2005), Age-progressive volcanism of the Oregon High Lava Plains: Overview and evaluation of tectonic models, in *Plates, Plumes, and Paradigms*, edited by G. R. Foulger et al., *Spec. Pap. Geol. Soc. Am.*, *388*, 503–515.

Jordan, B. T., A. L. Grunder, R. A. Duncan, and A. L. Deino (2004), Geochronology of age-progressive volcanism of the Oregon High Lava Plains: Implications for the plume interpretation of Yellowstone, *J. Geophys. Res.*, *109*, B10202, doi:10.1029/2003JB002776.

Jordan, T. H. (1979), Mineralogies, densities and seismic velocities of garnet lherzolites and their geophysical implications, in *The Mantle Sample: Inclusions in Kimberlites and Other Volcanics*, edited by F. R. Boyd and H. O. Meyer, pp. 1–14, AGU, Washington, D. C.

Kennett, B. L. N., and E. R. Engdahl (1991), Traveltimes for global earthquake location and phase identification, *Geophys. J. Int.*, *105*, 429–465, doi:10.1111/j.1365-246X.1991.tb06724.x.

Lerch, D. W., E. Miller, M. McWilliams, and J. Colgan (2008), Tectonic and magmatic evolution of the northwestern Basin and Range and its transition to unextended volcanic plateaus: Black Rock Range, Nevada, *Geol. Soc. Am. Bull.*, *120*, 300–311, doi:10.1130/B26151.1.

Lévêque, J. J., L. Rivera, and G. Wittlinger (1993), On the use of the checkerboard test to assess the resolution of tomographic inversions, *Geophys. J. Int.*, *115*, 313–318, doi:10.1111/j.1365-246X.1993.tb05605.x.

Marone, F., and B. Romanowicz (2007), Non-linear crustal corrections in high-resolution regional waveform seismic tomography, *Geophys. J. Int.*, *170*, 460–467, doi:10.1111/j.1365-246X.2007.03399.x.

Michaelson, C. A., and C. S. Weaver (1986), Upper mantle structure from teleseismic P-wave arrivals in Washington and northern Oregon, *J. Geophys. Res.*, *91*, 2077–2094, doi:10.1029/JB091iB02p02077.

Orr, E., W. Orr, and E. Baldwin (1992), *Geology of Oregon*, 4th ed., Kendal/Hunt, Dubuque, Iowa.

Pierce, K. L., and W. J. Morgan (1992), The track of the Yellowstone hotspot: Volcanism, faulting, and uplift, in *Regional Geology of Eastern Idaho and Western Wyoming*, edited by P. K. Link et al., *Mem. Geol. Soc. Am.*, *179*, 1–53.

Pierce, K. L., L. A. Morgan, and R. W. Saltus (2000a), Yellowstone plume head: Postulated tectonic relations to the Vancouver slab, continental boundaries and climate, *U.S. Geol. Surv. Open File Rep., 2000–498*, 39 pp.

Pierce, K. L., L. A. Morgan, and R. W. Saltus (2000b), Yellowstone plume head: Postulated tectonic relations to the Vancouver slab, continental boundaries and climate, *U.S. Geol. Surv. Open File Rep., 00–0498*, 39 pp.

Pollitz, F. F. (2008), Observations and interpretation of fundamental mode Rayleigh wavefields recorded by the Transportable Array (USArray), *J. Geophys. Res.*, *113*, B10311, doi:10.1029/2007JB005556.

Rasmussen, J., and E. Humphreys (1988), Tomographic image of the Juan de Fuca plate beneath Washington and western Oregon using teleseismic P-wave travel times, *Geophys. Res. Lett.*, *15*, 1417–1420, doi:10.1029/GL015i012p01417.

Ribe, N. M., and U. R. Christensen (1994), Three-dimensional modeling of plume-lithosphere interaction, *J. Geophys. Res.*, *99*, 669–682, doi:10.1029/93JB02386.

Ritsema, J., and R. M. Allen (2003), The elusive mantle plume, *Earth Planet. Sci. Lett.*, *207*, 1–12, doi:10.1016/S0012-821X(02)01093-2.

Saleeby, J., and M. Ducea (2003), Production and loss of high-density batholithic root, southern Sierra Nevada, California, *Tectonics*, *22*(6), 1064, doi:10.1029/2002TC001374.

Severinghaus, J., and T. Atwater (1990), Cenozoic geometry and thermal state of the subducting slabs beneath western North America, in *Basin and Range Extensional Tectonics Near the Latitude of Las Vegas, Nevada*, edited by B. P. Wernicke et al., *Mem. Geol. Soc. Am.*, *176*, 1–22.

Sigloch, K., N. McQuarrie, and G. Nolet (2008), Two-stage subduction history under North America inferred from multiple-frequency tomography, *Nat. Geosci.*, *1*, 458–462, doi:10.1038/ngeo231.

Sleep, N. H. (1990), Hotspots and mantle plumes: Some phenomenology, *J. Geophys. Res.*, *95*, 6715–6736, doi:10.1029/JB095iB05p06715.

Smith, R. B. (1977), Intraplate tectonics of western North American Plate, *Tectonophysics*, *37*, 323–336, doi:10.1016/0040-1951(77)90055-5.

Smith, R. B., and L. W. Braile (1994), The Yellowstone hotspot, *J. Volcanol. Geotherm. Res.*, *61*, 121–187, doi:10.1016/0377-0273(94)90002-7.

Spetzler, J., and R. Snieder (2004), The Fresnel volume and transmitted waves, *Geophysics*, *69*, 653–663, doi:10.1190/1.1759451.

Stachnik, J. C., K. Dueker, D. L. Schutt, and H. Yuan (2008), Imaging Yellowstone plume-lithosphere interactions from inversion of ballistic and diffusive Rayleigh wave dispersion and crustal thickness data, *Geochem. Geophys. Geosyst.*, *9*, Q06004, doi:10.1029/2008GC001992.

Steinberger, B. (2000), Plumes in a convecting mantle: Models and observations for individual hotspots, *J. Geophys. Res.*, *105*, 11,127–11,152, doi:10.1029/1999JB900398.

Takahahshi, E., K. Nakajima, and T. L. Wright (1998), Origin of the Columbia River basalts: Melting model of a heterogeneous plume head, *Earth Planet. Sci. Lett.*, *162*, 63–80, doi:10.1016/S0012-821X(98)00157-5.

Tikoff, B., and J. Maxson (2001), Lithospheric buckling of the Laramide foreland during Late Cretaceous and Paleogene, western United States, *Rocky Mtn. Geol.*, *36*, 13–35.

van der Lee, S., and G. Nolet (1997), Upper mantle S velocity structure of North America, *J. Geophys. Res.*, *102*, 22,815–22,838, doi:10.1029/97JB01168.

Vandecar, J. C., and R. S. Crosson (1990), Determination of teleseismic relative phase arrival times using multi-channel cross-correlation and least-squares, *Bull. Seismol. Soc. Am.*, *80*, 150–169.

Waite, G. P., D. L. Schutt, and R. B. Smith (2005), Models of lithosphere and asthenosphere anisotropic structure of the Yellowstone hot spot from shear wave splitting, *J. Geophys. Res.*, *110*, B11304, doi:10.1029/2004JB003501.

Waite, G. P., R. B. Smith, and R. M. Allen (2006), $V_P$ and $V_S$ structure of the Yellowstone hot spot from teleseismic tomography: Evidence for an upper mantle plume, *J. Geophys. Res.*, *111*, B04303, doi:10.1029/2005JB003867.

Wang, K., J. H. He, and E. Davis (1997), Transform push, oblique subduction resistance, and intraplate stress of the Juan de Fuca plate, *J. Geophys. Res.*, *102*, 661–674, doi:10.1029/96JB03114.

West, J. D., M. J. Fouch, J. B. Roth, and L. T. Elkins-Tanton (2009), Vertical mantle flow associated with a lithospheric drip beneath the Great Basin, *Nat. Geosci.*, *2*, 439–444, doi:10.1038/ngeo526.

Wilson, D. S. (1988), Tectonic history of the Juan de Fuca Ridge over the last 40 million years, *J. Geophys. Res.*, *93*, 11,863–11,876, doi:10.1029/JB093iB10p11863.

Xue, M., and R. M. Allen (2006), Origin of the Newberry Hotspot Track: Evidence from shear-wave splitting, *Earth Planet. Sci. Lett.*, *244*, 315–322, doi:10.1016/j.epsl.2006.01.066.

Xue, M., and R. M. Allen (2007), The fate of the Juan de Fuca plate: Implications for a Yellowstone plume head, *Earth Planet. Sci. Lett.*, *264*, 266–276, doi:10.1016/j.epsl.2007.09.047.

Yang, Y. J., and M. H. Ritzwoller (2008), Teleseismic surface wave tomography in the western U.S. using the Transportable Array component of USArray, *Geophys. Res. Lett.*, *35*, L04308, doi:10.1029/2007GL032278.

Yuan, H. Y., and K. Dueker (2005), Teleseismic P wave tomogram of the Yellowstone plume, *Geophys. Res. Lett.*, *32*, L07304, doi:10.1029/2004GL022056.

R. M. Allen, Department of Earth and Planetary Science, University of California, 307 McCone Hall, Berkeley, CA 94720, USA. (rallen@berkeley.edu)

M. Xue, State Key Laboratory of Marine Geology, School of Ocean and Earth Science, Tongji University, 1239 Siping Rd., Shanghai, China.